

## **IDENTIFICATION PERFORMANCE OF THE IMS IN THE MIDDLE EAST AND NORTH AFRICA**

**Terrance G. Barker  
G. Eli Baker  
Keith L. McLaughlin**

**Maxwell Technologies, Inc.  
8888 Balboa Avenue  
San Diego, CA 92123-1506**

**January 1998**

**Final Report  
8/10/95 – 8/9/97**

**Approved for Public Release; Distribution Unlimited**



**DEPARTMENT OF ENERGY  
Office of Nonproliferation and National Security  
WASHINGTON, DC 20585**

**AIR FORCE RESEARCH LABORATORY  
Space Vehicles Directorate  
29 Randolph Road  
AIR FORCE MATERIEL COMMAND  
HANSCOM AFB, MA 01731-3010**

**DTIC QUALITY INSPECTED 3**

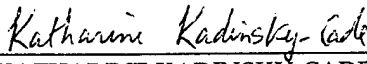
**19980928 050**


SPONSORED BY  
Department of Energy  
Office of Non-Proliferation and National Security

MONITORED BY  
Air Force Research Laboratory  
CONTRACT No. F19628-95-C-0111

The views and conclusions contained in this document are those of the authors and should not be interpreted as representing the official policies, either express or implied, of the Air Force or U.S. Government.

This technical report has been reviewed and is approved for publication.

  
KATHARINE KADINSKY-CADE  
Contract Manager

  
CHARLES P. PIKE, Deputy Director  
Integration and Operations Division

This report has been reviewed by the ESD Public Affairs Office (PA) and is releasable to the National Technical Information Service (NTIS).

Qualified requestors may obtain copies from the Defense Technical Information Center. All others should apply to the National Technical Information Service.

If your address has changed, or you wish to be removed from the mailing list, or if the addressee is no longer employed by your organization, please notify AFRL/VSOS-IM, 29 Randolph Road, Hanscom AFB, MA 01731-3010. This will assist us in maintaining a current mailing list.

Do not return copies of the report unless contractual obligations or notices on a specific document requires that it be returned.

REPORT DOCUMENTATION PAGE			Form Approved OMB No. 0704-0188	
Public reporting burden for this collection of information is estimated to average 1 hour per response, including the time for reviewing instructions, searching existing data sources, gathering and maintaining the data needed, and completing and reviewing the collection of information. Send comments regarding this burden estimate or any other aspect of this collection of information, including suggestions for reducing this burden, to Washington Headquarters Services, Directorate for Information Operations and Reports, 1215 Jefferson Davis Highway, Suite 1204, Arlington VA 22202-4302, and to the Office of Management and Budget, Paperwork Reduction Project (0704-0188), Washington, DC 20503.				
1. AGENCY USE ONLY (Leave blank)		2. REPORT DATE January 1998		3. REPORT TYPE AND DATES COVERED Final (8/10/95 - 8/9/97)
4. TITLE AND SUBTITLE Identification Performance of the IMS in the Middle East and North Africa			5. FUNDING NUMBERS Contract No. F19628-95-C-0111 PE 69120H PR DENN TA GM WU AC	
6. AUTHOR(S) Terrance G. Barker, G. Eli Baker, Keith L. McLaughlin				
7. PERFORMING ORGANIZATION NAME(S) AND ADDRESS(ES) Maxwell Technologies, Inc. Federal Division 8888 Balboa Avenue San Diego, CA 92123-1506			8. PERFORMING ORGANIZATION REPORT NUMBER  MFD-DTR-98-15600	
9. SPONSORING/MONITORING AGENCY NAME(S) AND ADDRESS(ES) Air Force Research Laboratory 29 Randolph Road Hanscom AFB, MA 01731-3010 Contract Manager: Katharine Kadinsky-Cade/VSBS			10. SPONSORING/MONITORING AGENCY REPORT NUMBER  AFRL-VS-HA-TR-98-0032	
11. SUPPLEMENTARY NOTES This research was sponsored by the Department of Energy, Office of Nonproliferation and National Security, Washington, DC 20585				
12a. DISTRIBUTION/AVAILABILITY STATEMENT  Approved for public release; distribution unlimited			12b. DISTRIBUTION CODE	
13. ABSTRACT (Maximum 200 words)  We have simulated the detection and identification performance of the proposed seismic network of the International Monitoring System (IMS) in the Middle East/North Africa. Figure 1 shows a map of Africa and western Eurasia with the proposed IMS alpha stations and the area for which the simulations were done. The identification performance of a network is strongly dependent upon regional source and propagation variability. However, knowledge of those variations permits estimation of their impact on the effectiveness of discriminants throughout the region. A comprehensive compilation of source and propagation properties was made and used to simulate network identification performance using the Monte Carlo program Xnice. The simulations described here include a greater area (northwestern Africa) and use a far more extensive Continued . . .				
14. SUBJECT TERMS Seismology      Test Ban Treaty      Network Simulation			15. NUMBER OF PAGES 56	
			16. PRICE CODE	
17. SECURITY CLASSIFICATION OF REPORT Unclassified	18. SECURITY CLASSIFICATION OF THIS PAGE Unclassified	19. SECURITY CLASSIFICATION OF ABSTRACT Unclassified	20. LIMITATION OF ABSTRACT SAR	

**UNCLASSIFIED**

SECURITY CLASSIFICATION OF THIS PAGE

CLASSIFIED BY:

**N/A since Unclassified.**

DECLASSIFIED ON:

**N/A since Unclassified.**

13. ABSTRACT (Continued)

set of source and propagation parameters than our previous work (Barker, 1996). We find that the predicted performance of the Lg/P ratio and Lg slope discriminants ranges from extremely poor to extremely well within the study area, a result of the distribution of source propagation characteristics and station coverage.

In another set of simulations, we have investigated the relationship between confidence ellipses estimated by the event location procedure and the distribution of locations found by the procedure. We find that the confidence ellipses are underestimates of the location variance.

SECURITY CLASSIFICATION OF THIS PAGE

**UNCLASSIFIED**

## TABLE OF CONTENTS

Section	Page
1 Introduction .....	1
2 Source and Propagation Properties in the Middle East and North Africa.....	3
2.1 Source Excitation .....	3
2.2 Attenuation and Blockage .....	3
3 Simulations of Detection and Identification Performance .....	17
4 Monte Carlo Versus Formal Location Uncertainties .....	30

## FIGURES

Figure		Page
1	Locations of shots (circles) and recorders (triangles) relative to shot 167 .....	2
2	Events and stations used to estimate source and propagation parameters .....	4
3	Paths for which Lg is clearly observed .....	5
4	Paths for which Lg is not observed despite clear P arrivals and low noise levels .....	5
5	Paths for which Sn is clearly observed .....	6
6	Paths for which Sn is not observed despite clear P arrivals and low noise levels .....	6
7	Seismogram of an event on the Saudi shield recorded at HALM (a Saudi shield station) .....	7
8	Events occurring within and on the African side of the Red Sea, and recorded at Saudi shield stations .....	8
9	Envelope record section of Red Sea events recorded at the Saudi station RANI, arranged by distance from the Red Sea axis toward the Saudi shield. ....	8
10	Events labeled 1 through 10 are those shown in Figure 9 .....	10
11	Image of $m_b$ (P) detection thresholds for the proposed IMS network .....	18
12	Image of $m_b$ (Lg) detection thresholds for the proposed IMS network .....	19
13	Contours of log moment (Nt-m) detection levels for the proposed IMS network.....	20

# FIGURES (continued)

Figure		Page
14	Image of Q at 1 Hz for Lg.....	17
15	Image of Lg source excitation relative to central Arabian Shield .....	22
16	Contours of fraction of events identified as earthquakes by the Lg/P discriminant at $m_b = 3.5$ for the proposed IMS network.....	23
17	Contours of fraction of events identified as earthquakes by the Lg/P discriminant at $m_b = 4.0$ for the proposed IMS network .....	24
18	Contours of fraction of events identified as earthquakes by the Lg/P discriminant at $\log m_0 = 14.0$ for the proposed IMS network.....	25
19	Contours of fraction of events identified as earthquakes by the Lg/P discriminant at $\log m_0 = 15.0$ for the proposed IMS network.....	26
20	Contours of fraction of events identified as earthquakes by the Lg discriminant at $m_b = 4.0$ for the proposed IMS network.....	27
21	Contours of fraction of events identified as earthquakes by the log slope discriminant at $\log m_0 = 14.0$ for the proposed IMS network .....	28
22	Contours of fraction of events identified as earthquakes by the log slope discriminant at $\log m_0 = 15.0$ for the proposed IMS network .....	29
23	Monte Carlo locations for 35N, 40N, and 45N at 85W for $m_b(\text{Lg}) = 3.5 \pm 0.1$ .....	32
24	Monte Carlo locations and formal confidence ellipses for 35N, 40N, and 45N at 85W for $m_b(\text{Lg}) = 3.5 \pm 0.1$ .....	33
25	Map showing contours of the percentage of true locations contained within the formal errors of a Monte Carlo simulation of synthetic events with $3.0 < m_b(\text{Lg}) < 4.2$ .....	34
26	Comparison of the normalized cumulative errors to those predicted by a best fitting Chi-squared distribution.....	35

## 1.0 Introduction

Monitoring a CTBT requires accurate assessments of how well the monitoring networks detect and identify seismic events. The computer program **Xnice**, for **N**etwork **I**dentification **C**apability **E**valuation running under an **X**-windows interface, has been written by Maxwell Technologies to assess the ability of a seismic network to identify seismic sources. The program simulates the detection, location and identification of populations of events recorded on regional and teleseismic networks using a Monte Carlo approach. This approach allows isolation of the effects of source type, propagation path, and choice of discriminants on the discrimination process. In addition, discriminant performance and network thresholds of detection, location and identification are assessed. **Xnice** generates the parameters of a sequence of events and computes the ground motions from the events at the stations of the network. The features of the ground motions used for discrimination are then measured, and discrimination scores are assigned to each event. From a suite of events, the performance of the network and the discriminants can be assessed. The program has the capability to compute signals from earthquakes, quarry blasts and both overburied and normally buried explosions.

Under programs jointly sponsored by DoD and DoE, data on the source and propagation characteristics of the Middle East and North Africa have recently been compiled. These data were used to simulate earthquakes and explosions in this region and then assess the identification performance of proposed IMS Alpha stations (Figure 1). This is a complicated area with several regions of Lg blockage. We show magnitude and moment levels at which identification can be made and expected success rates.

This report consists of three major sections. The first describes source and propagation characterization for network performance simulations in the Middle East. Accurate network performance simulation depends on accurate characterization of regionalized source and propagation parameters. To improve network performance simulation in the Middle East, we have incorporated new and previously determined Middle East seismic propagation and source parameters into the **Xnice** simulation software (Barker, 1996). Results and implications of the simulations are discussed in the second section of this report. The last section of this report focuses on location errors, using **Xnice** simulations to investigate formal location uncertainties.

These results demonstrate both the power of the **Xnice** program to simulate network detection and identification performance in a complex region, and the need for comprehensive compilations of source and propagation characteristics to infer accurate network performance characteristics.



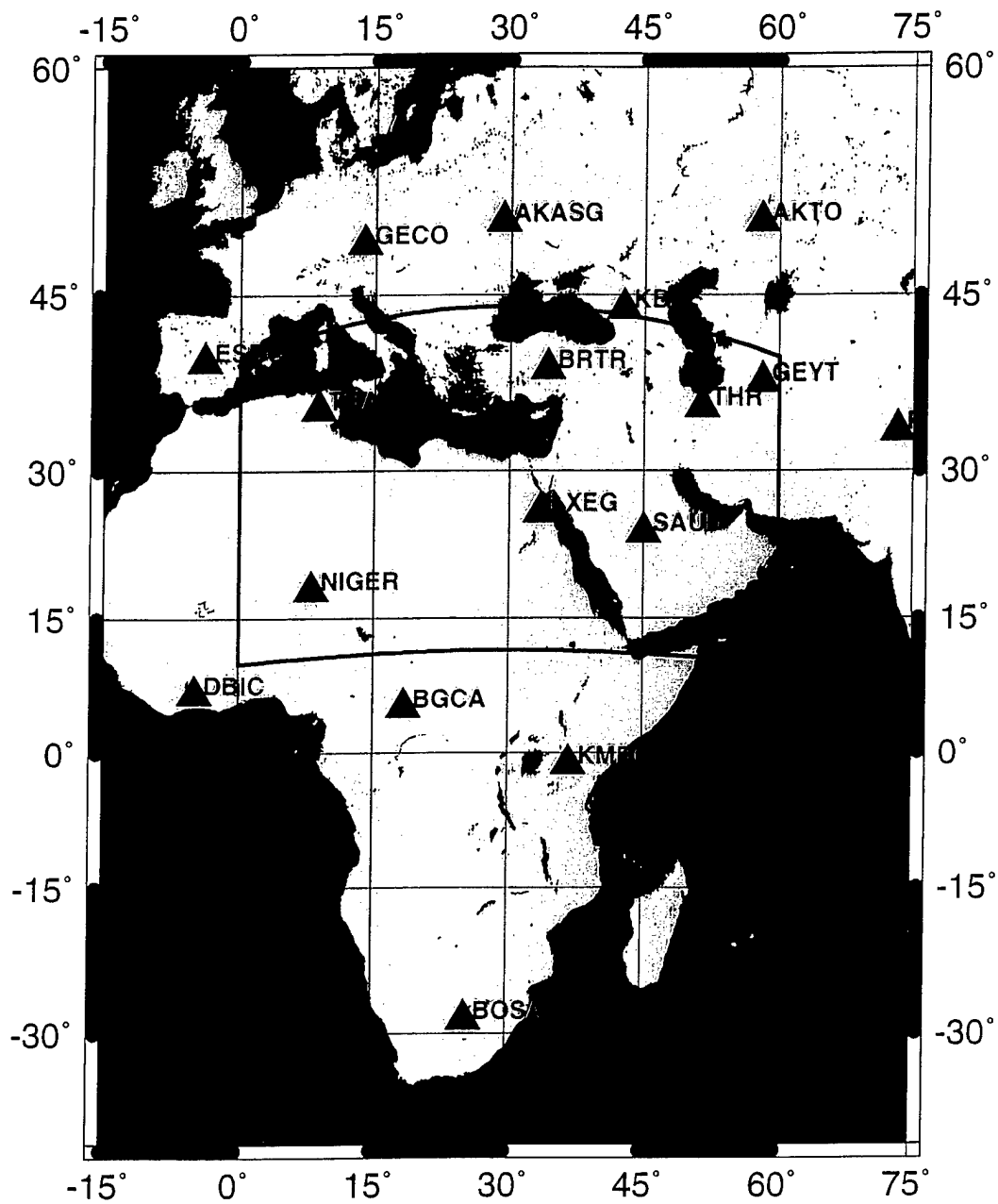


Figure 1-1. Proposed IMS seismic stations and study area.

## 2.0 Source and Propagation Properties in the Middle East and North Africa

### 2.1 Source Excitation.

The first part of this section concentrates on the determination of source excitations, and on crustal and upper mantle attenuation characteristics. Source excitations predict the amplitude that will be observed in a signal from a particular region for a given event magnitude (assuming the propagation parameters are also known).

We analyze regional phases from distinct source areas in and around the Saudi Shield, the Turkish and Iranian Plateau, the adjacent Arabian, Mediterranean, Black, and Caspian Seas, and the western edge of the Hindu-Kush (Figure 2). Data come from two sets of stations, with no temporal overlap. One set comes from a broadband array deployed on the Saudi shield (Vernon *et al.*, 1996) and permanent IRIS and GEOSCOPE broadband stations. The other data set comes from historical SRO and Iranian Long-Period Array records, obtained from the Ground Truth Data Base (GTDB) web site (Grant *et al.*, 1996). The two sets are linked by a large number of events from a common region, the Zagros. Wherever possible, the source excitation for each of Pn, Pg, Sn, and Lg, is estimated for each region. A conservative estimate of variations between regional source excitations indicates an expected factor of 15 variation regionally in Lg amplitudes for events of the same magnitude, independent of propagation effects. Where high signal to noise ratio recordings are available for a wide range of frequencies, we determine the frequency dependence of the source excitations. For events in the Zagros, Pn and Sn excitations are frequency independent from 0.6 to 15 Hz. That contrasts with excitations, variously of Pn, Pg, and/or Lg, from the Gulf of Aqaba, the Arabian shield, the Arabian Sea, and eastern Turkey, which decrease with frequency.

Source excitations trade-off with attenuation, which must be determined independently. For the crust, we use  $Q_0$  and  $\eta$  values determined from Lg coda (Mitchell *et al.*, 1997), with adjustments where indicated by our increased data coverage. Where no other information is available, we use mantle  $Q_0$  values twice those of the overlying crust.

A cluster of events that span the Red Sea provides a unique set of observations of the transmission of energy between Lg and Sn. The shear-wave energy from events nearest the Saudi shield arrives at Saudi stations in the Lg phase. For events somewhat further from the Saudi shield, with paths crossing more of the Red Sea, the Lg phase is still observed, but some shear-wave energy arrives as Sn. Recordings at Saudi stations of Red Sea events farthest from the Saudi shield have no Lg, only Sn.

### 2.2 Attenuation and Blockage

To characterize source regions, we must account for propagation effects. To that end, we incorporate attenuation parameters from Mitchell *et al.* (1997) and Xie and Mitchell (1990). Mitchell has provided us with their most up to date estimates of frequency dependent  $Q$  in Africa and Eurasia. We have augmented and refined these models where additional data permit. Rodgers *et al.* (1997) examined Lg and Sn

propagation for paths in the northern part of the map in Figure 2. Their extensive study, particularly in Iran, but also in propagation to ANTO and KIV, confirms and augments our observations, and better constrains propagation effects so that we can effectively estimate source excitations.

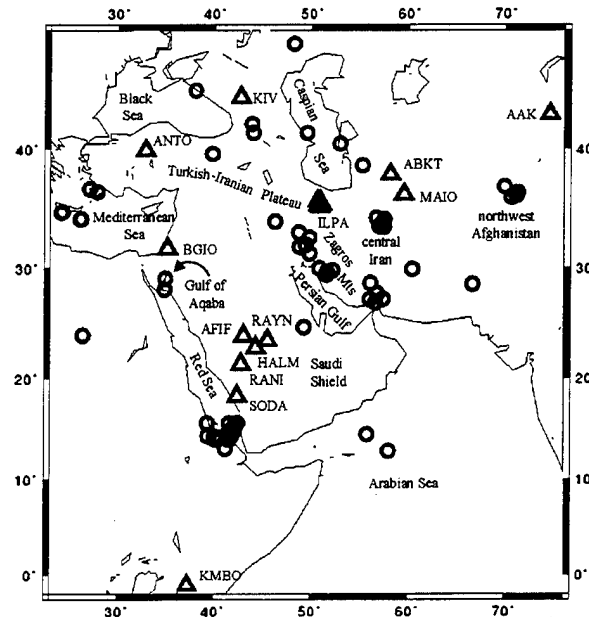


Figure 2. Events (circles) and stations (triangles) used to estimate source and propagation parameters. All events are assumed to be crustal based on PDE and/or regional network bulletin depths. Distinct features are labeled.

Figures 3 through 6 indicate paths for which Lg and Sn are, and are not, observed. There are several areas where Lg is blocked, including areas of oceanic crust, e.g. the Red Sea, the Arabian Sea, the Black Sea, and the Mediterranean Sea. Other seas with deep sediments block Lg as well, including the Persian Gulf and the Caspian Sea. In those cases, the blockage is not as clearcut. For example, a low frequency signal ( $<0.25$  Hz), does appear in the Lg window for Zagros events recorded on the Saudi Shield, from which we infer an Lg  $Q_0$  of  $\sim 30$  in the Persian Gulf. There is also distinct Lg for paths both entirely within and crossing into the Turkish-Iranian Plateau, although for long paths across the plateau Lg is not observed, which is consistent with the low Lg  $Q_0$  of  $\sim 200$  found by Mitchell *et al.* (1997). While Lg does not propagate across the Caspian or Black Seas, it does propagate between them. This observation was previously noted by Baumgardt (1996). Lg is also observed at MAIO for a nearby event east of the Caspian Sea, but is not observed from a slightly more distant event. Figures 5 and 6 for these events show that Sn is clearly observed from all events in the Black/Caspian Sea region, except for those two from which Lg is observed. This highlights an important consideration for future implementations of network simulations, which is the desirability of the ability to define regions with arbitrary boundaries. There is no consistency in Lg observations propagating north from the Zagros. Some events have clear Lg while nearby events have none.

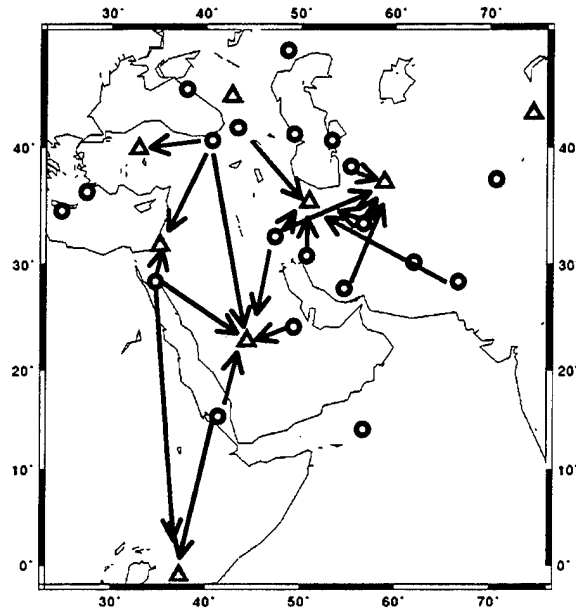


Figure 3. Paths for which Lg is clearly observed (solid lines). For clarity a single circle is drawn for each source region. Similarly, one triangle represents the five stations within the Saudi shield, the adjacent stations ABKT and MAIO, and the stations of the ILPA array.

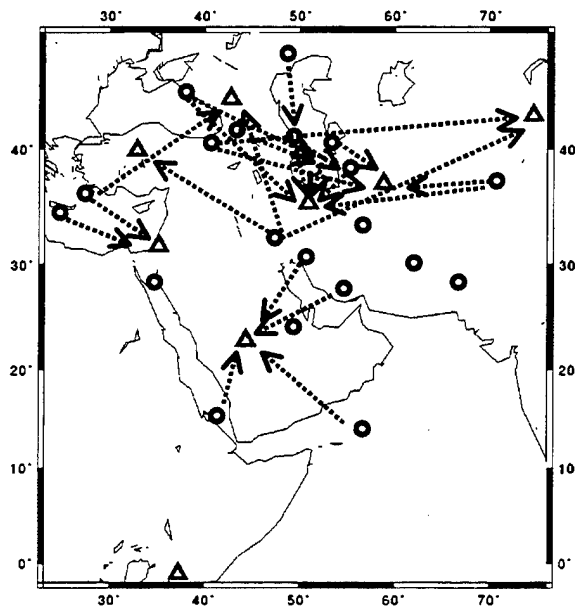


Figure 4. Paths for which Lg is not observed (dashed lines) despite clear P arrivals and low noise levels. Even so, abrupt blockage is not necessarily implied for each path. Some paths, particularly in the northern part of the map may indicate low crustal Q throughout entire path lengths. Paths from the southern Red Sea region to the Saudi Shield are drawn both here and in Figure 2. A consistent and interesting pattern in this region, which is too fine scale for the maps above, is detailed in Figures 7-9. The event north of the Caspian Sea was a nuclear explosion, for which Lg presumably was small.

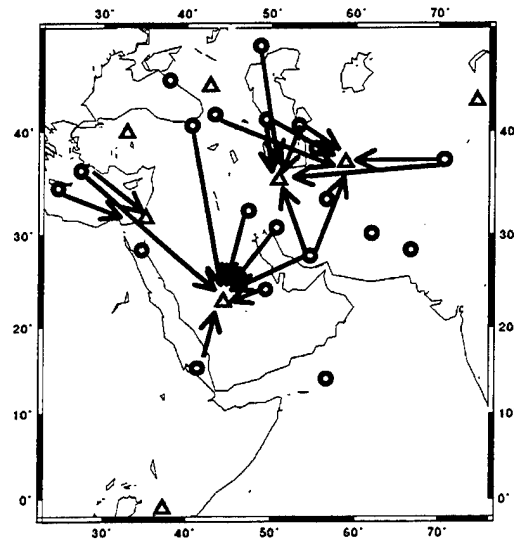


Figure 5. Paths for which Sn is clearly observed (solid lines).

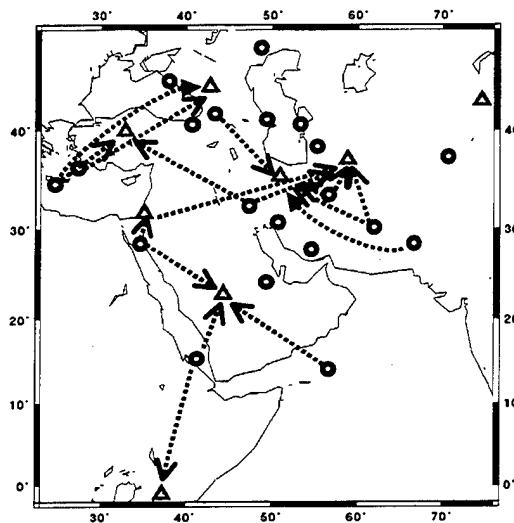


Figure 6. Paths for which Sn is not observed (dashed lines) despite clear P arrivals and low noise levels. As was the case for Lg, paths from the southern Red Sea region to the Saudi Shield are drawn both here and in Figure 5. Details are shown in Figures 8-10.

In many regions Lg and Sn are mutually exclusive phases for particular paths. That is commonly the case here, although both phases are observed for some paths. In the southern Red Sea, we see that whether Lg, Sn, or both, are observed at Saudi stations depends on the distance of the event from the shield (Figures 8-10). This highlights the difficulty of parameterizing structurally and tectonically complex regions on the coarse scale necessary for complete global coverage.

Both Lg and Sn are observed from events with paths entirely within the Saudi shield, although the passbands in which Lg and Pg are observed have practically no overlap with the passbands in which Sn and Pn are observed (Figure 7). This underscores

a point that is important to event identification under a CTBT. *Which P-phase and which S-phase are being used for discrimination must be considered.* Simply using whichever phase is observed or largest (i.e. Pn vs. Pg and Sn vs. Lg) can lead to errors in discrimination, particularly with spectral discriminants. For example, for recordings at approximately  $10^\circ$  we commonly observe either Pn and Lg, which have very different spectra, or Pn and Sn, which usually have similar spectra, as illustrated in Figure 7.

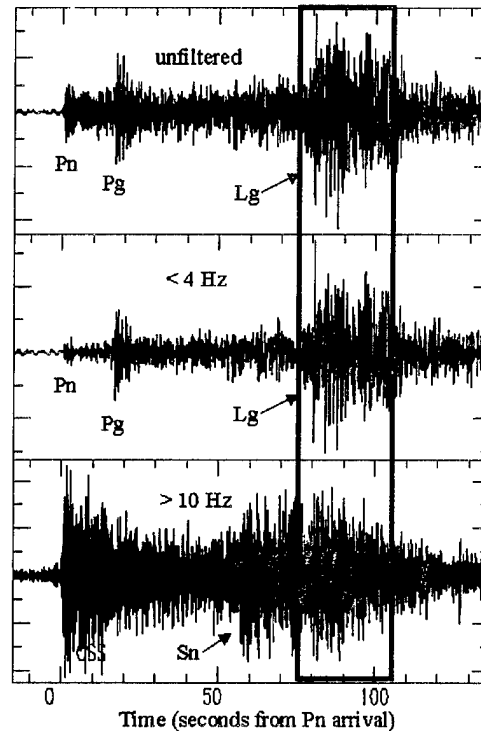


Figure 7. Seismogram of an event on the Saudi shield recorded at HALM (a Saudi shield station). Pn, Pg, and Lg (group velocity window is delineated by vertical lines) are clear in the top (unfiltered) and middle (lowpass filtered below 4 Hz) traces. The bottom trace (highpass filtered above 10 Hz) show Pn and Sn dominating at higher frequencies.

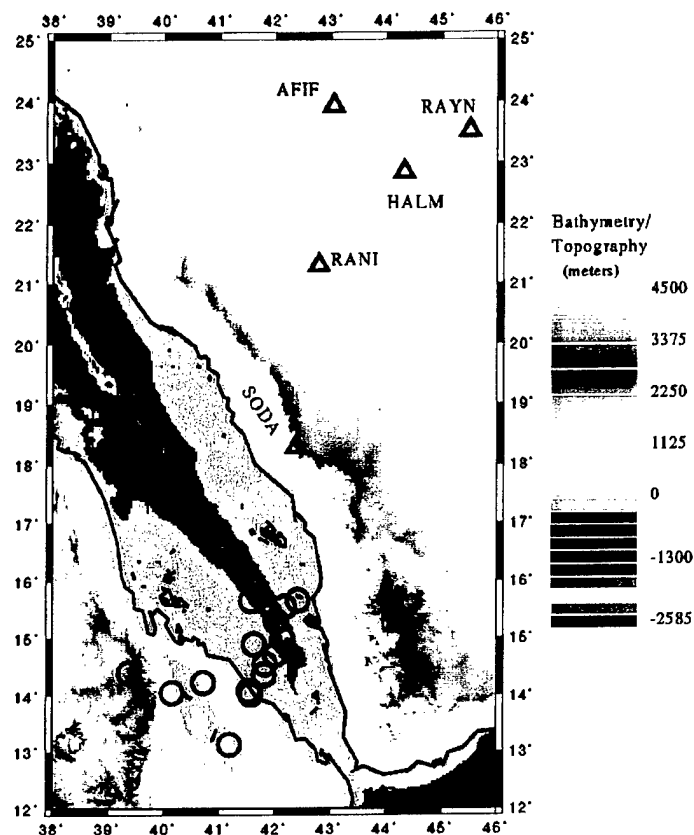


Figure 8. Events (circles) occurring within and on the African side of the Red Sea, and recorded at Saudi shield stations (triangles).

The appearance of Lg vs. Sn on the Saudi shield appears to be a function of distance the shear wave energy must traverse across the oceanic crust of the Red Sea to stable continental crust. This is illustrated with a record section of events recorded at one station. Record sections of events recorded at other stations are very similar.

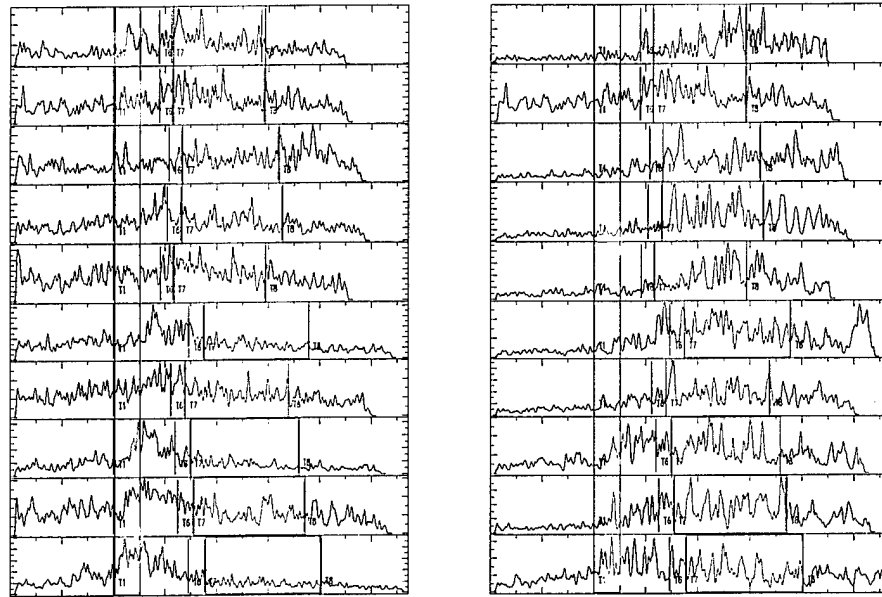


Figure 9. Envelope record section of Red Sea events recorded at the Saudi station RANI, arranged by distance from the Red Sea axis toward the Saudi shield. Events corresponding to each trace number are shown in Figure 10. Two passbands are used, 2-6 Hz (left), and 0.4-2 Hz (right), as Lg and Sn are typically dominated by different frequencies. For easier observation the envelope functions are smoothed by two passes of a one-second triangle function. The traces are aligned by the predicted Sn arrival time (first vertical line). The second vertical line marks the beginning of the pre-Lg noise window at 3.7 km/sec, and the next two vertical lines delineate the beginning and end, at 3.6 and 3.0 km/sec, of the Lg window. There is a gradual transition from the top trace to the bottom (from events nearer the Saudi shield to events nearer to or in Africa) from the dominance of Lg, to the dominance of Sn. The arrival times also shift with distance. For example, Sn arrives at the predicted Sn time for event 10, but arrives successively later for events 9, 8, 7, and 6, at some point looking more like early Lg than late Sn.



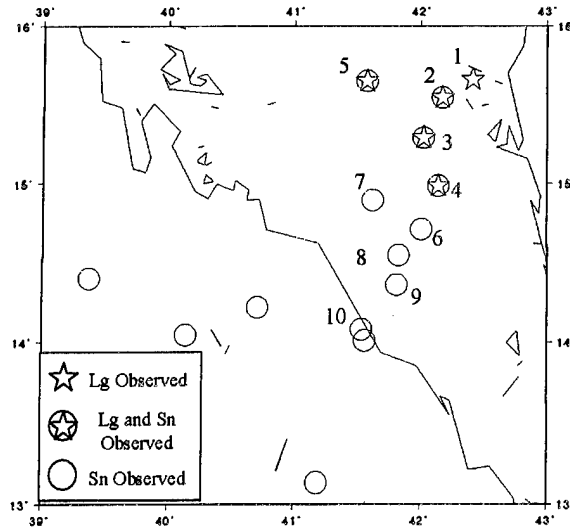


Figure 10. Events labeled 1 through 10 are those shown (from top to bottom) in Figure 9. For events shown as stars, Lg is observed at Saudi shield stations with peak amplitude in the 1-2 Hz passband more than twice that in the pre-Lg window. For those shown as circles peak Sn amplitude is more than twice that in the pre-Sn window (to avoid clutter, the pre-Sn window is not shown in Figure 9). For events shown as stars within a circle, both phases are observed with greater than two times the pre-phase noise window amplitudes.

The propagation paths within the Red Sea of the earthquakes in Figures 8 and 10 are likely in oceanic crust, although there is a transition southward to continental crust beginning somewhere around  $16^\circ$  (e.g. Gettings *et al.* 1986). There are at least two simple possible explanations of the observations noted in Figure 8. One is that Lg propagates some short distance in the oceanic (or partially in extended continental) crust before leaking into the upper mantle and travelling as Sn. That would provide somewhat late starting initial arrivals for Sn. Another possibility is that there is essentially no Lg from the beginning for the oceanic crustal events, but that there is significant Sn-to-Lg conversion at the very abrupt oceanic-continental crust interface (e.g. Gettings *et al.* 1986). Again, with distance from the Saudi coastline, this would lead to later Sn (or earlier Lg) times. Also, with sufficient event distance from the oceanic-continental boundary, Sn could propagate deep enough to pass under that transition and so avoid conversion to Lg. We are currently testing these hypotheses with finite-difference synthetics.

#### Source Excitations for Pn, Pg, Sn, and Lg.

We have used the concept of source excitations (Barker, 1996) to parameterize source regions in a manner useful for network performance evaluation. The source excitation is the logarithm of the factor that predicts amplitude from  $m_b$ , relative to the amplitude predicted for that  $m_b$  at some reference location. That is, the log of the amplitude of a given phase should simply equal  $m_b$  plus a constant, given appropriate corrections for geometric spreading, attenuation, and source spectral shape. Amplitudes of any particular phase, however, vary depending on the source region. Likely causes for

this include variations in focal mechanism and depth, and in near source scattering and attenuation characteristics. The source excitation thus serves as a catchall factor for describing amplitude variations. Because they cover such a multitude of causes for amplitude variation, which are not likely to be well characterized globally in the near future, physical characteristics of the source and source region cannot be directly inferred from the source excitations. On the other hand, this concept enables a very practical statistical characterization of each source region, permitting predictions of amplitude at each station for each phase, given the IMS  $m_b$ . We present next the details of the source excitation estimation, the assumptions made, and the results obtained. We use IMS body wave magnitudes, which have been determined from maximum P-wave amplitudes recorded at greater than 20 degrees, with the peak typically between 1 and 2 Hz. We assume these magnitudes accurately reflect the amount of energy released from the source.

First we define a reference Lg amplitude that is tied to the IMS  $m_b$ . The path for the magnitude 3.68 event on January 7, 1996 is entirely within the Arabian Shield, and has a maximum Lg displacement of 117 nm at RAYN, the permanent IRIS station at a distance of 3.62 degrees. For comparison of amplitudes we scale all observations to  $10^\circ$  distance and  $m_b$  of 5.0. This scaling is done according to

$$\log_{10}(A_{mb=5.0}(10^\circ)) = 5.0 - mb + \log_{10}(A_{obs}(\Delta^0)) + \frac{5}{6} \log_{10}\left(A_{obs}\left(\frac{\Delta^0}{10^\circ}\right)\right) + 0.4343\left(\frac{\pi f^{1-\eta}}{U_g Q}\right) 111.19(\Delta^0 - 10^\circ).$$

$\Delta^0$  is distance,  $U_g$  is group velocity (3.5 km/sec for Lg),  $Q_0$  is the quality factor for attenuation, and  $\eta$  describes the frequency dependence of attenuation. We use  $Q_0=400$  and  $\eta = 0.5$  for the Saudi Shield. For this calculation we use  $f=1.4$  Hz, as this is the center of the measurement passband used. We employ the same filter and passband for this reference Lg amplitude measurement as is used for IMS amplitude measurements for  $m_b$  estimation. The fourth term on the right represents geometric spreading. The  $5/6$  comes from a value of  $1/2$  for any regional phase which propagates in 2 dimensions (along a surface) plus an additional  $1/3$  for Lg, due to the definition of its peak amplitude as an Airy phase (Nuttli, 1973). The reference event so scaled should have a  $\log_{10}$  amplitude of  $\log_{10}(A(10^\circ))=2.20$ , and source excitations for all other passbands and phases are relative to this value.

To estimate the predicted amplitude at the source, we must also correct for the shape of the source spectra. Because the  $m_b$  is based on amplitude at approximately 1.4 Hz, the amplitude predicted in the equation above is also valid for approximately 1.4 Hz. To estimate source excitation at other frequencies, we must account for the relative source spectral amplitudes at 1.4 Hz to the amplitudes at other frequencies of interest. Due to the source finiteness, high frequencies have lower amplitude in the far field. The Brune model (Brune, 1970) predicts decay in spectral amplitudes above the corner

frequency,  $f_c$ , proportional to  $\frac{1}{\omega^2}$ , as follows:  $\Omega(\omega) \propto \frac{f_c^2}{f_c^2 + \omega^2}$ . We predict corner frequencies using the dynamic modeling results of Madariaga (1976), in which

$f_c = 0.21 \frac{\beta}{a}$  for S-waves and  $f_c = 0.32 \frac{\beta}{a}$  for P-waves. This is consistent with the most accurate observational studies of the relationship between magnitude and corner frequency (e.g. Abercrombie, 1995).  $\beta$  is the shear wave velocity, and  $a$  is the characteristic dimension of the fault, defined by  $a = \left(0.44 \frac{M_0}{\sigma}\right)^{1/3}$ , where  $M_0$  is seismic moment, and  $\sigma$  is stress drop.

We assume  $\sigma=100$  bars throughout. Although some studies have indicated a dependence of stress drop on moment for events smaller than  $m_b=4.0$ , observations made at 2.5 km depth in crystalline granite conclusively demonstrate a constant stress drop down to  $M_L=-1.0$  (Abercrombie, 1995). To estimate the moment, we use the equation  $\log(M_0) = 1.5M_w + 16.1$  of Hanks and Kanamori (1979), where  $M_w$  may be  $M_L$ ,  $m_b$ , or  $M_s$ , depending on event size. This choice is consistent with the moment magnitude relation obtained for Israeli earthquakes by Shapira and Hofstetter (1993), of  $\log(M_0) = (1.5 \pm 0.1)M_L + (16.0 \pm 0.4)$ .

For each phase we estimate source excitations for the passbands measured by the IDC, which are 0.8-2 Hz, 2-4 Hz, 6-8 Hz, and 8-10 Hz. For greater accuracy we also estimate phase amplitudes at 0.3-0.6 Hz, 1-3 Hz, 3-5 Hz, 5-7 Hz, 7-9 Hz, 10-12 Hz, 11-13 Hz, 12-14 Hz, 13-15 Hz, and 14-16 Hz. The measurements are of maximum amplitude for each phase and for noise windows before each phase, with windows defined according to the IDC protocol. We were able to make the following minor modifications to the IDC definitions for this study, as individual inspection of records permits us to avoid misassociation errors. We use longer pre-phase windows (10 seconds rather than 3), ending earlier than the predicted phase arrival time. This provides more stable and conservative noise measurements and avoids erroneously large noise measurements due to early arriving phases. The IDC Pg window appears to end very early relative to observed Pg in the Middle East, so we use a Pg window ending at 5.6 km/s group velocity (the IDC definition is 5.8 km/sec). Further, the Sn window is taken to extend from the predicted arrival time until 3.7 km/s group velocity, as largest Sn amplitudes often occur more than 20 seconds after the predicted arrival time (which is the IDC definition of the Sn end time). Only measurements with a signal to noise ratio (S/N) greater than 3 were used. Because the behavior of the spectra is complicated near the corner frequency, we use source excitation estimates from passbands as far above and below the corner frequency as possible to define an empirical source excitation function,  $S(f)=S_0+S_1 \cdot f$ , for each region.  $S(f)$  is the  $\log_{10}$  of the amplification of each phase relative to the reference value.

Regions: In this section we describe the results of source excitation estimation for each region.

Saudi Shield: The excitations here are determined from the reference event, which by design will have an Lg excitation of  $\log_{10}(1)=0.0$  at 1.4 Hz. That is, the multiplicative correction factor for  $m_b$ -based predicted amplitudes will be 1.0. Sn was not observed for

this event at sufficiently high S/N to permit source excitation estimation. For Pn, the upper mantle attenuation parameters were set to  $Q_0=1000$  and  $\eta=0.9$ , as described in the southern Zagros discussion.

Arabian Sea: Despite low noise levels, no Sn was observed from these events, so Sn excitation,  $S_{Sn}$  was set to  $S_{Pn}-0.7$ , where  $S_{Pn}$  is the Pn source excitation. This provides that the Sn amplitude will be 1/5 of the Pn amplitude, assuming similar attenuation.

Zagros: Events from the Zagros are used to compare excitations determined from the two distinct data sets, that from current permanent stations and the Saudi array, and that from ILPA and the old SRO station MAIO. Assuming that propagation effects are well characterized, excitations *should* be the same regardless of which sets of stations are used in their estimation. In practice, site amplifications can vary significantly between stations, (e.g. Su *et al.*, 1992) which could bias excitation estimates. Further, this comparison provides a check on the conversion from counts to nanometers, about which we had some doubts for the older data set. It is therefore encouraging to see that estimates from the two data sets, for Pn excitation, were similar. The Pn excitations (the best and most consistently recorded phase for both data sets) in the northern and southern Zagros were both estimated to be -0.55 using the newer data (corresponding to 0.28 of the reference amplitude). Pn excitations estimated from the ILPA and MAIO data averaged -0.37 (corresponding to 0.43 of the reference amplitude). More events were observed at ILPA and MAIO, and they indicate some variation in excitation from south to north.

Events from the southern Zagros recorded at the Saudi shield have large Pn and Sn phases out to very high frequency. Using  $\eta=0.5$  for the mantle for the paths to the Saudi stations, even with  $Q_0=1000$ , would result in a factor of 20 increase in Pn and Sn source excitations from 1.0 to 15 Hz for these events. Although a precise physical interpretation of source excitations is unsettled, we can see no simple explanation that explains such an increase with frequency. Thus we use a high upper mantle  $\eta$  of 0.9, with a  $Q_0$  of 1000, comparable to values in eastern North America (Nuttli, 1973). In that case, the median source excitations are nearly flat across all frequencies.

Pn for events from the northernmost Zagros is also well recorded at Saudi stations out to 15 Hz (the highest frequency measured), with no indication of frequency dependence of excitation (assuming the same attenuation parameters as above). The variance of Pn and Sn source excitations does increase at the lowest frequencies. This presumably is because the events have predicted corner frequencies, where the source spectral shape becomes complicated, ranging from 0.34 to 1.17 Hz. For purposes of prediction, we use a flat source excitation (i.e.  $S_1=0$ ). The narrower passband recorded, and ambiguity over the frequency response of the ILPA and MAIO instruments restricted those observations to periods near 1 Hz.

Paths to the Saudi shield from the southern Zagros cross the sedimentary basin of the Persian Gulf, which appears to block both Lg and Pg, as neither phase is observed in the passbands examined. Neither phase propagates northward either, where crustal attenuation is high. For the frequency bands of interest, we use the same Pg and Lg

excitation as found for the northern Zagros, because of the similarities between the regions, including comparable Pn and Sn excitations.

A low frequency Lg phase begins to emerge from the noise in Saudi recordings of southern Zagros events, at  $\sim 3.2$  km/s at 4 seconds period, and becomes more prominent at longer period. We use this observation, and assume most attenuation takes place in the Persian Gulf, to infer an approximate Lg  $Q_0$  of 30 in the Persian Gulf.

The cluster of events in the central Zagros all belong to the ILPA and MAIO data set. Pn and Sn excitations are consistent with those of the southern Zagros. Just four Lg observations were also made, but because of doubts about propagation characteristics, discussed below, the inferred excitations of -0.3 are dubious.

The Pg and Lg paths for the northernmost Zagros events to the Saudi stations cross a deep sedimentary basin west of the Zagros, which may significantly diminish crustal phase amplitudes and could bias the source excitation estimates downward. Pg is not observed on the Saudi shield for these events, but is observed at ILPA and MAIO. To estimate Lg excitation using the Saudi shield data, we use  $Q_0$  of 250, as an average of values along the path, as Mitchell *et al.* (1997) found an average  $Q_0$  of 200 north of the Arabian shield, and Lg  $Q$  is likely lower in the sedimentary basin. The Lg observed at the shield sites is quite late, so we use a group velocity of 3.2 km/sec, rather than the typical value of 3.5 km/sec. Only the lowest frequencies of Lg were observed, so no estimate of frequency dependence could be made. These parameters lead to an excitation estimate of 0.2 at 0.6 Hz, corresponding to amplitudes approximately 1.6 times larger than the reference value. Just two Lg observations were also recorded at ILPA and MAIO from events in the same area. Those observations also lead to an excitation estimate of 0.2. Thus concern over the sketchiness of the Lg excitation estimates is somewhat allayed by their consistency for different paths and stations. Observations of Lg at ILPA and MAIO however are extremely intermittent, with most events not recording significant amplitudes. We suspect that Lg blockage is occurring for many of the paths, but with high spatial variability in its effectiveness due to the structural complexity and topographic roughness of the Zagros and the Iranian Plateau. The practical effect is that the variability in propagation is mapped into a high variance for the source excitations.

East-central Iran (and further east): Pn and Sn were well recorded from the central Iran events and consistently found to be near the reference amplitude. The results were the same for the 2 events in southeastern Iran and in Pakistan.

Pn arrivals were also consistently observed from the mountainous region of northwest Afghanistan, at slightly higher than reference amplitudes (Pn excitation = 0.2). Sn was also observed (with Sn excitation = -0.15), but only at MAIO, not at ILPA. This could be due to poor Sn propagation throughout the Iranian Plateau, as noted by Rodgers *et al.* (1997).

Caspian and Black Seas: The events within and near these inland seas all recorded clear Pn arrivals at LIPA and MAIO, most of which had small amplitudes (Pn excitations of

-0.6). Lg blockage occurs for paths crossing either sea, but recordings at ILPA of events between the two seas have clear Lg, which indicate Lg excitation of -0.7.

Eastern Turkey: Events from this and the other remaining regions were recorded on the Saudi array and at permanent IRIS stations. Pn and Lg are observed from the event in eastern Turkey. There appears to be some decrease in Pn source excitation with frequency, although interpretation is difficult due to the low corner frequency of this  $m_b=4.9$  event ( $f_c=1.1$ ). Lg is very prominent at lower frequencies. Pn, Sn, and Lg amplitudes, corrected for propagation, are much greater in the Saudi shield than elsewhere. This could be due to the much greater structural complexity on other paths, as is reflected in the smooth topography only along the path to the Saudi stations.

Southwest Turkish Coast: Only the mantle phases are observed from these events, and those only at lower frequencies. These provide a tentative indication of frequency dependence of excitation, but cover too small of a range to be conclusive. These events appear to occur just offshore, but could be on the continental shelf. As we have no information about Lg, except that it is not observed, we will for now assume Lg and Pg excitations that are somewhat smaller those of the mantle phases.

Crete: Although there is a hint of frequency dependence in the Pn measurements, it is not strong enough to use, and we use a constant Pn excitation of -0.4. Sn is only well recorded at BGIO. No Lg or Pg phases are observed.

Gulf of Aqaba: All phases but the rarely observed  $S_N$  for these 3 events indicate some frequency dependence. The variance of Pn excitations is high, but a moderate slope of excitation with frequency is apparent. As the data at higher frequencies are fewer, and lower signal to noise level, we purposely underestimate the slope, thus splitting the difference between choosing a constant vs. choosing frequency dependence. This is the case with much of the data, and we take the conservative approach in all regions, of moderating the slope, to avoid predicting erroneous extreme values.

Southern Red Sea: These events present an interesting set of observations, as illustrated in Figures 7-9. Events within the Red Sea appear to be located on a transform fault, such as discussed in El-Isa and Shanti (1989). As the source excitation is currently determined for each  $5^\circ \times 5^\circ$  region, we use an average of all the values.

Table 1. Regionalized source excitations. Asterisks identify values assumed for phases not observed. These are assumed to be  $S_{Pn}-0.7$ , unless otherwise constrained, as discussed in the text. Average values are given for the entire Black and Caspian Sea region, although some small geographic variations exist (the double asterisk indicates that Lg excitation was only measured for events between the two seas, which had an unobstructed path to ILPA). The finer scale differences are incorporated into the model for Xnice calculations.

Region	Pn excitation	Pg excitation	Sn excitation	Lg excitation
SW Turkey Coast	0.0	-0.7*	0.0	-0.7*
Crete	-0.40	-1.1*	0.08	-1.1*
Gulf of Aqaba	-0.50-0.05·f	0.53-0.17·f	0.0	1.6-0.36·f
southern Red Sea	-0.8	-1.5*	-0.3	0.2
Arabian Sea	-0.29-0.10·f	-1.09*	-1.09*	-2.0*
Saudi Shield	-0.64	-0.11-0.13·f	-1.34*	0.38-0.27·f
southern Zagros	-0.55	-1.25*	-0.31	0.2*
central Zagros	-0.55	-1.25*	-0.46	0.2
northern Zagros	-0.0	0.4	-.046*	0.2
east-central Iran	0.0	0.1	-0.7*	0.2*
Northwest Afghanistan	0.2	-0.3*	-0.15	0.2*
Black and Caspian Sea	-0.60	-1.1*	-1.1*	-0.7**
eastern Turkey	0.09-0.17·f	-0.78·f*	0.11-0.17·f*	1.3

In the following section, we use these parameters to make simulations of IMS detection and identification performance in this region.

### 3.0 Simulations of Detection and Identification Performance

The IMS network proposed by the Conference on Disarmament Experts working Group in August, 1995 is more dense in the Middle East than that which is currently in place. We have performed simulations of the network's performance using **Xnice**. The details of the program and its use are given in Barker (1996). We briefly describe the simulation process here. We begin with a grid of source and propagation properties, as described in the previous section. At each point on a grid of source locations, we generate a suite of events and compute the expected signals at the stations in the network. The events are computed for a sequence of scalar moments at equal intervals of log moment. Care must be taken at this point to insure an adequate range of log moment values. For each moment, a number of realizations (40, for the calculations described here) of source stress drop, propagation noise and ground noise are made. The signal spectra are stored and analyzed for discrimination properties (e.g., network  $m_b$ ,  $Lg/P$ ). The results are written to a discrimination bulletin, and various other diagnostic files are generated, such as a file containing station statistics. This run is usually done in a batch mode, as it is rather time consuming. A subsequent module queries the user for what information he would like to extract from the discrimination bulletin and writes the results to a file and generates a figure, if requested. For the contour plots shown here, the user requests spatial distributions of thresholds or fractions of events satisfying a particular criterion, such as those detected or those identified by a particular set of discriminants. The program fits a Gaussian curve to the distribution of events satisfying the requested criterion, and reports the results for each source grid point. Finally, a map is made by contouring or otherwise imaging the grid.

The calculations presented here used the following parameters:

Mean stress drop	10 Mpa (100 bars)
Standard deviation of log stress drop	0.5
Minimum source depth	5km
Maximum source depth	15km
Standard deviation in propagation error	Lg 0.3, P 0.26, Pn 0.26, Pg 0.25, S 0.19, Sn 0.3
$Q_0$ for magnitudes	Lg 400, Pg 400, Pn 1000, Sn 1000
$\eta$ for magnitudes	Lg 0.5, Pg 0.5, Pn 0.9, Sn 0.9

Noise spectra for the SAUD station were obtained from analyses of pre-event noise at nearby stations in the data collected by Vernon *et al.* (1996). Noise levels at other stations were those collected for the **Xnice**/NetSim database (McLaughlin *et al.*, 1997).

An image of predicted  $m_b(P)$  detection thresholds for the proposed network is shown in Figure 11. Detection is based on the criteria used in GSETT-3 and currently implemented at the IDC. The rules are based on a weighted sum of travel time, azimuth and slowness measurements (J. Carter, Center of Monitoring Research, personal communication). Variations in  $m_b$  thresholds are due to variations in source excitation (as described above) and array geometry. Thresholds increase towards the southern part of the Arabian peninsula.



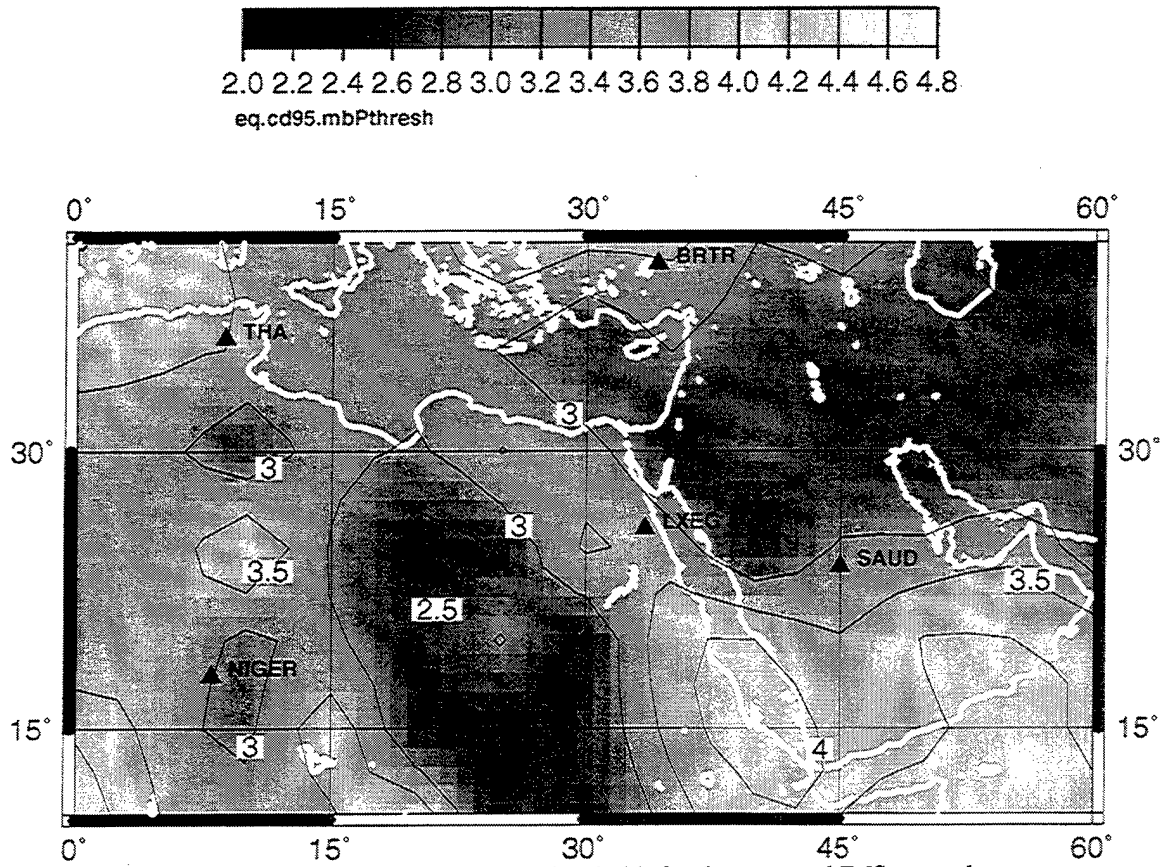


Figure 11. Image of  $m_b(P)$  detection thresholds for the proposed IMS network.

Detection thresholds for  $m_b(Lg)$  are shown in Figure 12. Thresholds are high in the southern part of the Arabian peninsula and low in Libya. This figure illustrates a problem in interpreting a magnitude threshold. A low threshold at a location is generally interpreted to indicate that smaller events can be detected there. However, the low  $m_b$  threshold in the southern part of the Arabian peninsula corresponds to events with larger moment. The following equations explain this. Regional amplitudes are calculated according to a relation (Barker, 1996) which we write as

$$A_i = S_0 P_1(\Delta) M_0,$$

where  $M_0$  is the seismic moment,  $S_0$  is the source excitation (essentially the amplitude for  $M_0 = 1$  at a reference distance) and  $P_1$  is a propagation operator incorporating geometric spreading and anelastic attenuation. As discussed above, the amplitudes for this region are quite variable and we set the parameters of the **Xnice** simulation to accurately predict amplitudes there. In an automatic monitoring environment, regional magnitudes will be assigned using a uniform magnitude distance relation, which can be parameterized by

$$m_b = \log(c P_2^{-1}(\Delta) A_i),$$

where  $c$  is a variable which does not depend on distance. To be consistent with this practice, magnitudes are computed this way in **Xnice**. Combining the two relations above, we have

$$m_b = \log(cS_0 M_0 P_1(\Delta) P_2^{-1}(\Delta)).$$

Thus, in source region where the source excitation is low, threshold values of  $m_b$  will be low (for a given  $M_0$ ). Threshold values of  $m_b$  will also be low if the path is attenuative relative to the uniform value ( $P_1/P_2 < 1$ ).

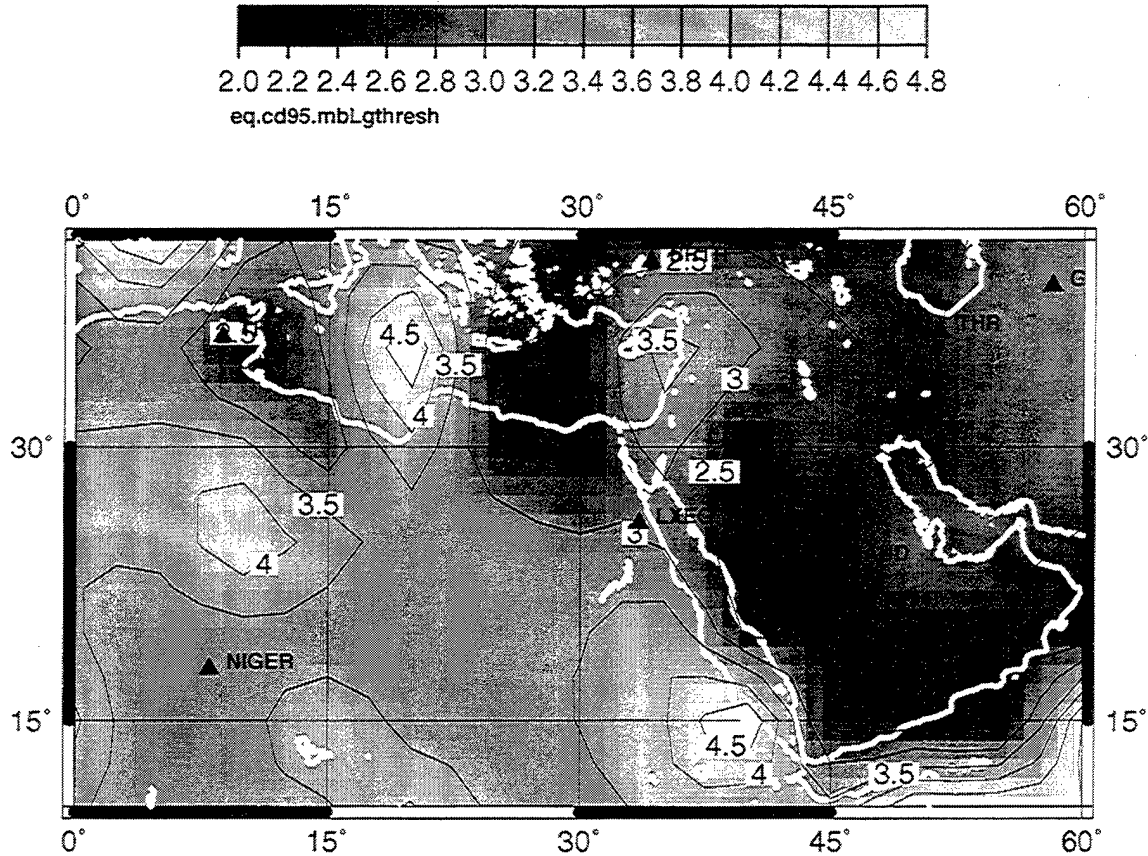


Figure 12. Image of  $m_b$  (Lg) detection thresholds for the proposed IMS network.

It is instructive to compare the magnitude detection thresholds in Figures 11 and 12 with the moment thresholds in Figure 13. Moment thresholds are high in the southern part of the Arabian peninsula and low in Libya, in contrast to the magnitude thresholds. Note the large range in moment threshold values from  $10^{12.5}$  to  $10^{17.5}$  Nt-m.

Much of the variability in threshold values is due to very low Lg Q values surrounding the region which prohibit signals reaching the requisite 3 stations, as exemplified by Lg Q shown in Figure 14 (see discussion in Section 2). Lg blockage (modeled in Xnice by zones of very low Q) prevents Lg measurements at the stations LXEG and NIGER from many source regions. Similarly, very low Q in the Persian Gulf and the sediments to the north of the Gulf prevent Lg energy from reaching THR. Even for purely continental paths, the low Lg Q of  $\sim 200$  greatly attenuates Lg signals traveling to BRTR.

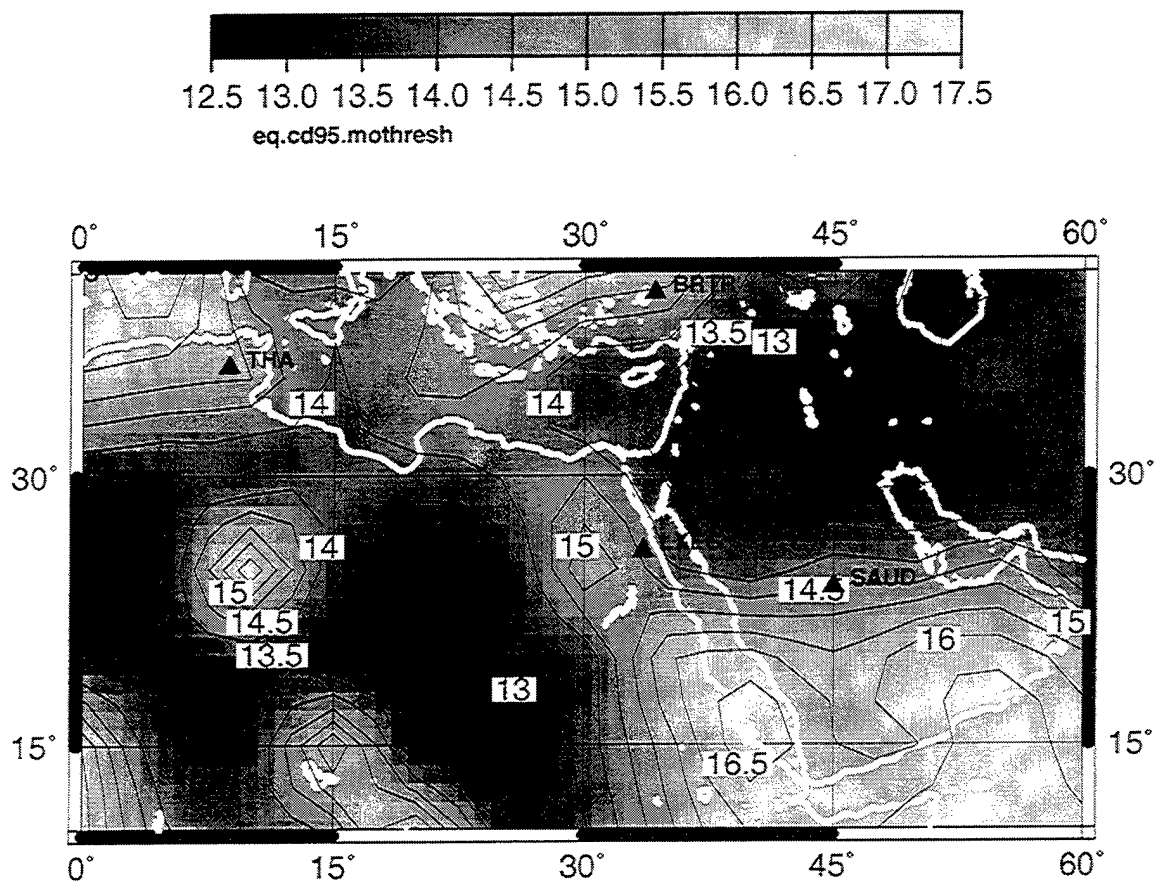


Figure 13. Contours of log moment (Nt-m) detection levels for the proposed IMS network.

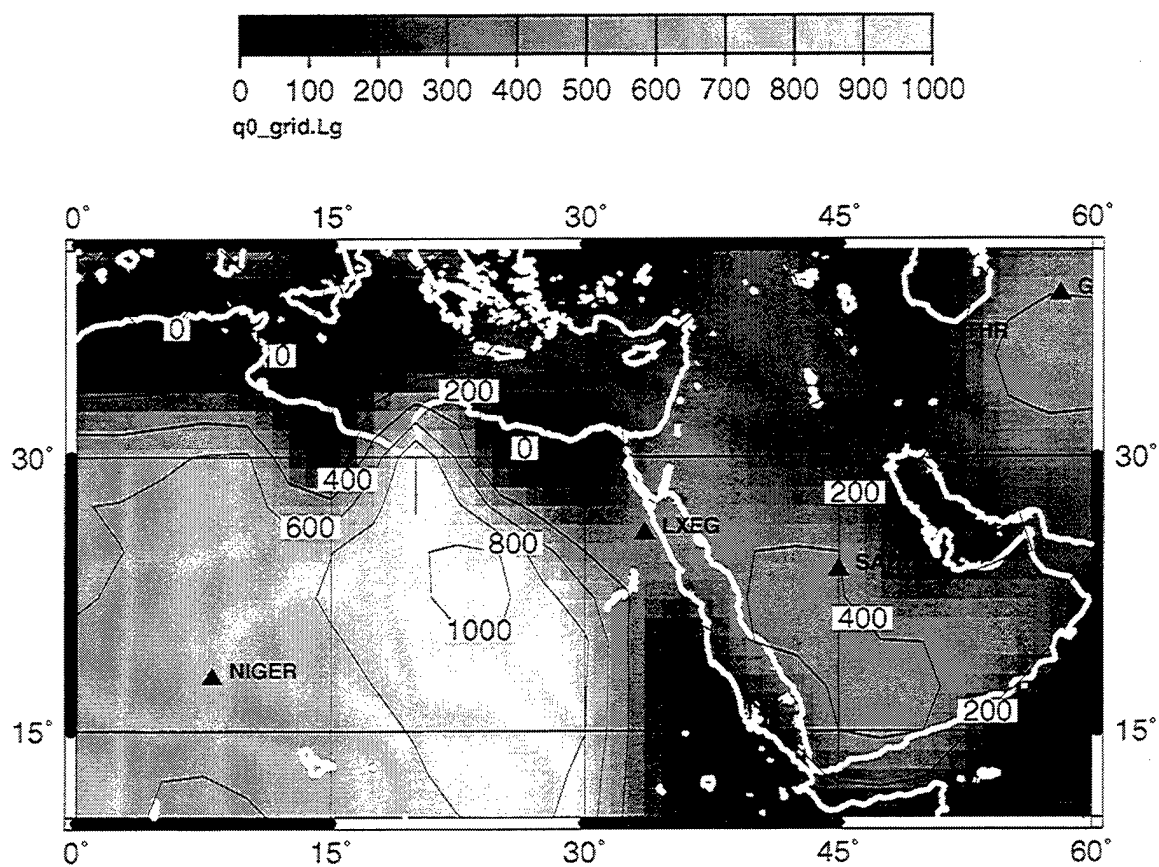


Figure 14. Image of Q at 1 Hz for Lg. Low Lg Q north of the Arabian Shield, very low Q in the Persian Gulf and blockage in the Red Sea prevent detections of Lg by the requisite 3 stations from events in the southern part of the shield.

Variability within the region is also due to variations in source strength. This is described in detail in Section 2 and summarized in Figure 15 for the Lg phase. The greatest variation occurs along the southern coast of the Mediterranean Sea.

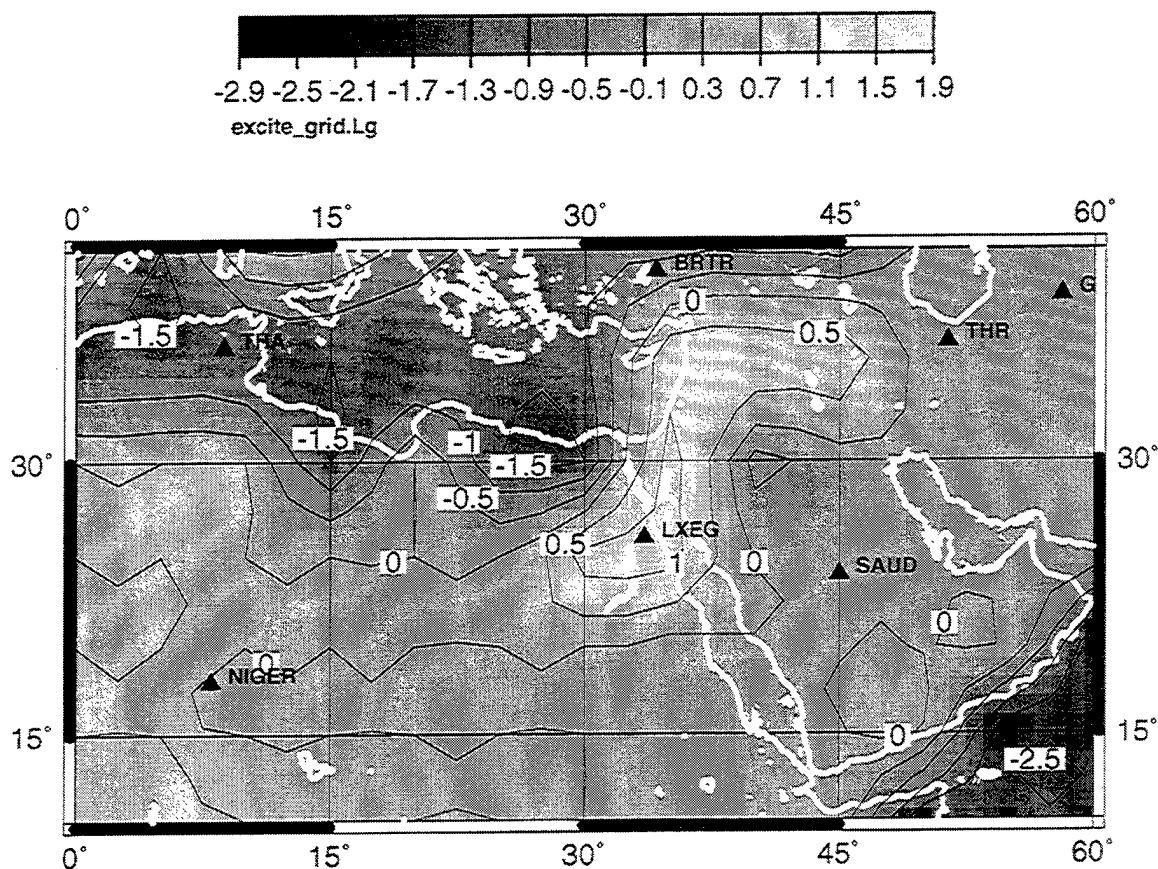


Figure 15. Image of Lg source excitation relative to central Arabian Shield.

We turn now to identification performance. We note first that teleseismic depth discriminants are ineffective because events in this region (and the simulation) are typically shallow ( $<10$  km). We did not model the  $M_s:m_b$  discriminant because we need accurate estimates of long-period noise for the networks, which we currently do not have. Thus, for events occurring on-shore, we must rely on regional discriminants for identification. Since small events are not detected (in the sense of the GSETT-3 rules) by the current IMS network in this region, teleseismic discrimination cannot be done. On the other hand, the proposed network is capable of regional discrimination. We consider first the Lg/P discriminant. An event is considered identified as an earthquake if (1) the event satisfies the event detection criterion, (2) both Lg and Pn or Pg exceed the signal-to-noise ratio at least 1 station, and (3) the Lg/P ratio exceeds a specified value (in this case, the value is zero). The fraction of events identified as earthquakes by the Lg/P discriminant at  $m_b=3.5$  is contoured in Figure 16.

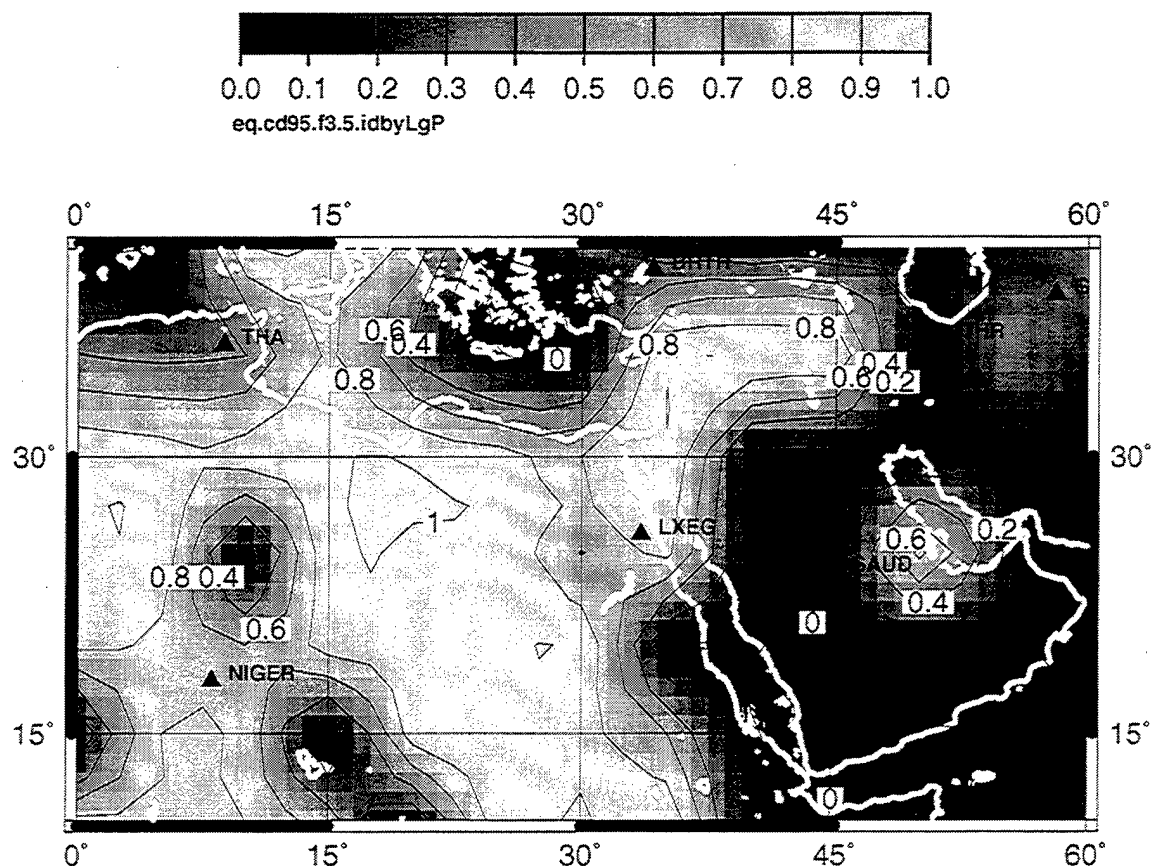


Figure 16. Contours of fraction of events identified as earthquakes by the Lg/P discriminant at  $m_b=3.5$  for the proposed IMS network. The decision line is  $\log(Lg/P) = 0.0$ .

For a larger magnitude,  $m_b=4.0$ , the performance is not greatly increased, as seen in Figure 17. For the Saudi peninsula, this is partly due to sparse station coverage (insufficient regional detections).

The identification performance is strongly influenced by the Q distribution. The poor performance of Lg/P in the Saudi peninsula is caused by (1) poor Lg detection and (2) by diminished Lg/P ratios due to propagation which attenuates Lg more than Pn. Identification levels for Lg/P at a fixed moment ( $\log M_0=14$ ), rather than fixed  $m_b(Lg)$ , are shown in Figure 18. The levels at  $m_b=4.0$  are comparable to those for  $\log M_0=14$  in northeast Africa away from the Red Sea, but are much less in the Saudi shield. Figure 19 shows identification levels for Lg/P at a higher fixed moment ( $\log M_0=15$ ). The performance is not significantly improved in the Saudi peninsula, indicating poor regional station coverage.

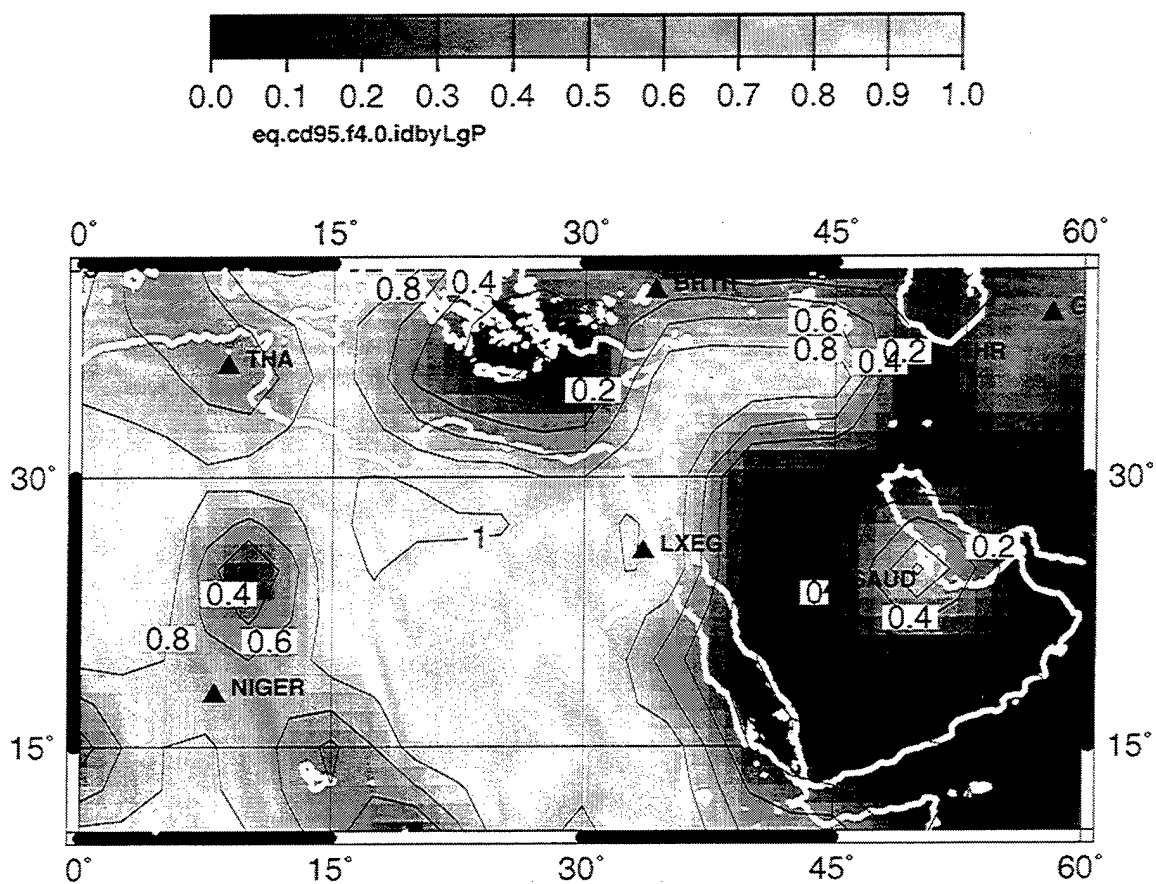


Figure 17. Contours of fraction of events identified as earthquakes by the Lg/P discriminant at  $m_b=4.0$  for the proposed IMS network. The decision line is  $\log(Lg/P) = 0.0$ .

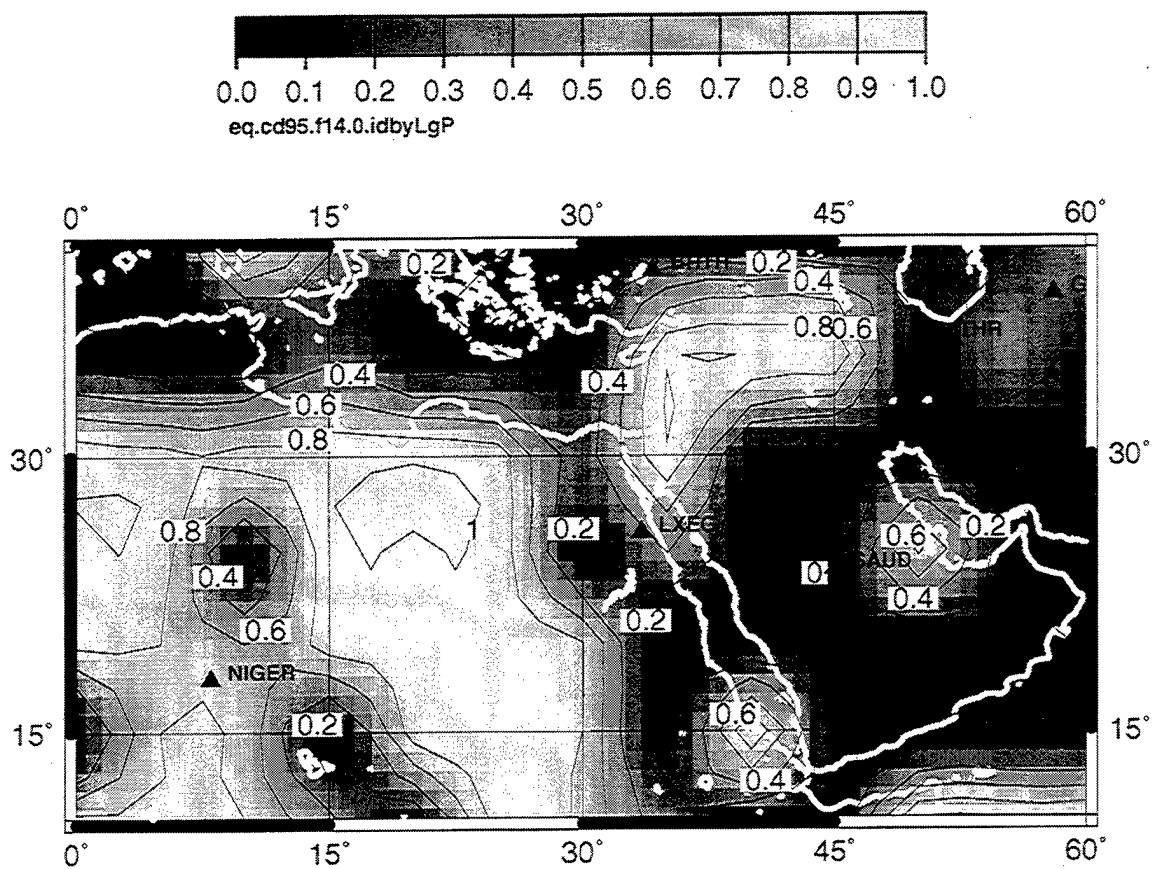


Figure 18. Contours of fraction of events identified as earthquakes by the Lg/P discriminant at  $\log M_0 = 14.0$  for the proposed IMS network. The decision line is  $\log(Lg/P) = 0.0$ .



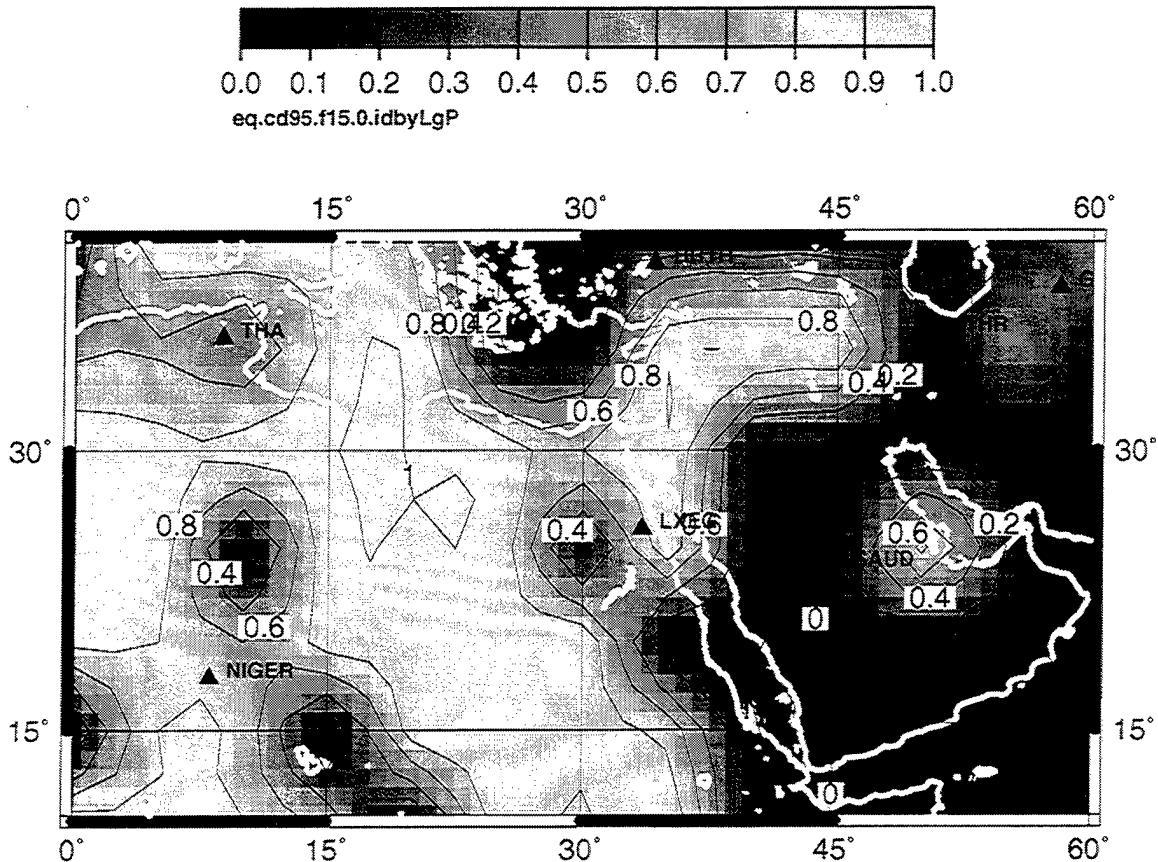


Figure 19. Contours of fraction of events identified as earthquakes by the Lg/P discriminant at  $\log M_0=15.0$  for the proposed IMS network. The decision line is  $\log(Lg/P) = 0.0$ .

We consider next the Lg slope discriminant, in which shallow spectral slopes are judged to be earthquake-like and steeper slopes explosion-like. Figure 20 shows the fraction of earthquakes with  $m_b=4.0$  identified as such by this discriminant, and Figure 21 shows the fraction of identified events at  $\log M_0=14$  and 15, respectively. This discriminant requires detection of a single phase (Lg), but detection is required for frequencies up to 8 Hz. As with Lg/P, the Lg excitation is a controlling feature for performance of this discriminant. In addition, since higher frequency detection is needed,  $Q(Lg)$  is an additional controlling feature. Thus, as seen in Figures 21 and 22, performance is best where Lg excitation and  $Q$  is high, and worst where they are low or where station coverage is poor (southern Saudi peninsula).

Each of the stations proposed in this region is very important to identification performance. Due to lack of coverage southeast of SAUD (in the Arabian Sea), this station is essential for monitoring the Arabian shield and the Sinai peninsula. Without station LXEG, there are no regional detections in northern Africa and stations THR and GEYT are needed for regional detections south of the Caspian Sea.

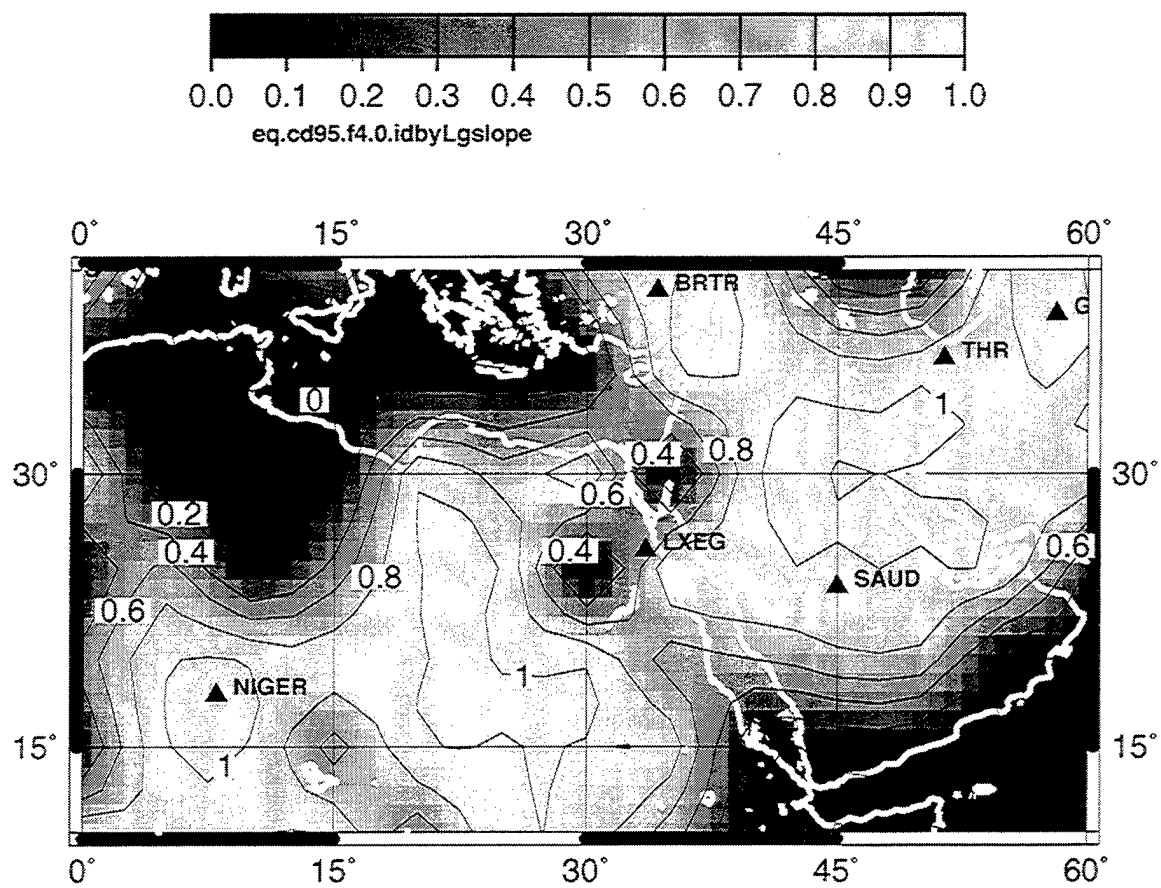


Figure 20. Contours of fraction of events identified as earthquakes by the Lg slope discriminant at  $m_b(Lg)=4.0$  for the proposed IMS network.

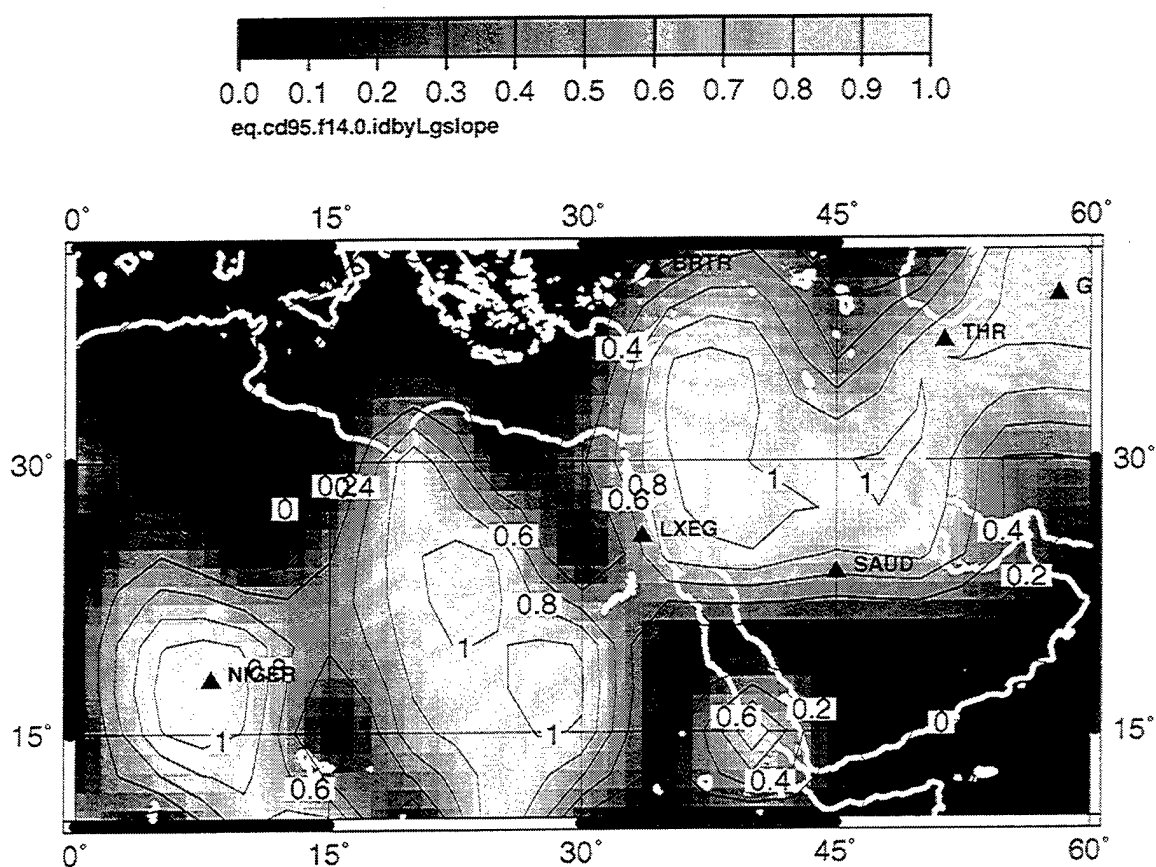


Figure 21. Contours of fraction of events identified as earthquakes by the Lg slope discriminant at  $\log M_0=14.0$  for the proposed IMS network. A comparison with Figure 20 demonstrates the importance of understanding the difference between moment and magnitude in evaluating network performance.

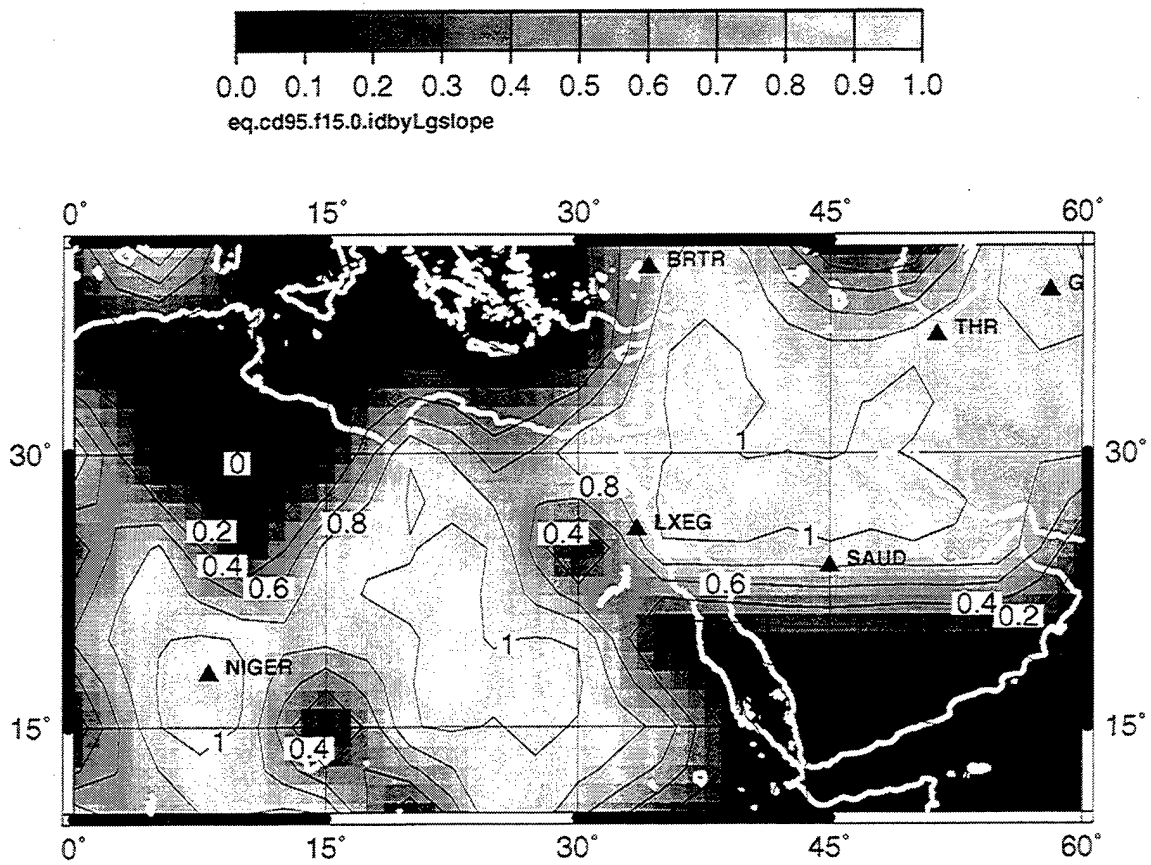


Figure 22. Contours of fraction of events identified as earthquakes by the Lg slope discriminant at  $\log M_0=15.0$  for the proposed IMS network. Compare with Figures 20 and 21.

#### 4. Monte Carlo Versus Formal Location Uncertainties

In this section, we compare two methods for estimating network location capability. The first method tabulates estimated location covariances from a Monte Carlo ensemble of event realizations. The second method tabulates formal location errors from a Monte Carlo ensemble of event realizations. To isolate aspects of the location procedure from effects due to source and propagation variation and station coverage, we have used the USNSN stations and events in the eastern U.S. In this region, stations are dense and well distributed, and propagation characteristics are relatively uniform.

Automatic earthquake epicenter location is normally treated as a non-linear least squares (NLLSQ) estimation procedure. The location is estimated by a step-wise minimization of a linearized least-squares estimator. At each step the location is perturbed to minimize an objective function composed of a weighted sum of the squares of the travel time residuals. The objective function is a non-linear function of the location. In the linearized formulation, the objective function is replaced by a Taylor series expansion at each iteration. The new source location is chosen to minimize the truncated series. The procedure iterates until a minimum in the objective function is found (least squares).

The first derivatives are zero at the minimum of the objective function, and it is assumed that the function is well represented by a quadratic form. Under these assumptions, error estimates for the epicenter location are derived using the curvature (second derivatives) of the objective function and the data variances. This formulation reduces to an equation for the location covariance matrix,  $\Sigma = (A^T A)^{-1} \sigma^2$ , where  $A$  is a matrix of derivatives of the individual station-phase travel times with respect to distance and  $\sigma^2$  is a normalized data variance. We refer to location error estimates derived from this formal linearization procedure as "formal errors." The formal covariance estimates,  $\Sigma$ , depend only upon the "curvature matrix,"  $(A^T A)^{-1}$ .

Since the objective function is non-linear, the shape of the function near the minimum may depart from a simple quadratic form. Under these conditions the estimated location covariance matrix may be an underestimate of the true location covariance. This assumption may be tested by comparing the ensemble of Monte Carlo locations with the predicted location errors.

Figure 23 a,b and c shows a Monte Carlo ensemble of  $m_b(Lg)=3.5 \pm 0.1$  events generated for three locations in the Midwest. The 90% confidence error ellipse derived from the population of Monte Carlo errors is shown on each plot. Each Monte Carlo realization was generated by adding Gaussian random numbers to the predicted travel times and then locating the event. A full Monte Carlo procedure was used.

- 1) Synthetic events with uniformly distributed moment from  $10^{10}$  to  $10^{15}$  Nt-m, and a log-normal distributed stress drop of 100 bars and a 50% standard deviation were generated on a grid of locations.

2) Spectral amplitudes of P, Pn, Pg, Sn, and Lg phase arrivals were computed at all stations for each event.

3) Probability of detection of each phase arrival was calculated using a statistical noise model at each station, 95% station reliability, and log-normal phase amplitude variability of 50% standard deviation.

4) Realizations of phase detection were selected for each event based on the predicted probabilities.

5) Travel times for each detected phase of each event realization were computed and a Gaussian random variable was added with standard deviations of 1.5, 2.5, 3.5, and 5.5 sec for P, Pg, Sn, and Lg respectively.

6) Location and location error was estimated for each event using Pn, Pg, Sn, and Lg travel times.

7) Network  $m_b(\text{Lg})$  was computed for each event from the detected Lg phase amplitudes.

8) Finally, each detected event was added to the synthetic location bulletin.

Figure 23 a,b and c shows 90% confidence error ellipses based upon analysis of the Monte Carlo errors defined as the difference between synthetic location and true location. This analysis assumes errors are Chi-squared distributed with two degrees of freedom, or equivalently as two independent Gaussian random deviates along the semi-major and semi-minor axes of the error ellipse. Under these assumptions, the  $X \times 100\%$  confidence error ellipse should contain  $N \times X \pm S$  of the  $N$  events in the Monte Carlo ensemble, where the standard deviation  $S^2 = N \times (X \times (1-X))$ . In contrast to confidence ellipses estimated in this manner we can examine location ellipses estimated from each realization.

Figure 24 a,b and c shows examples of 90% formal error ellipses from synthetic locations. There are far too many of them to examine them in detail, but we can see that the ellipses tend to be elongated along the same general direction as the scatter in estimated locations. We expect 90% of the 90% confidence ellipses to contain the true location. In fact we find only 80% to 85% of the ellipses contain the true location. This discrepancy is common for selected locations around the network. Formal 90% confidence ellipses are underestimated at selected locations within the USNSN network. Simple tests of significance verify that these are not due to sample variability. The Monte Carlo populations are large enough to distinguish when formal 90% confidence ellipses differ significantly from the Monte Carlo derived 90% confidence ellipses. No places in the network were found where the converse was true. While in most locations, the formal errors appear to be consistent with the Monte Carlo errors, there are no places where the formal error bounds are larger than the Monte Carlo error bounds.

This tendency for formal error ellipses to underestimate the 90% confidence region is illustrated in Figure 25. Contours are shown for the percentage of so-called 90% confidence ellipses that contain the true location for events between  $m_b(\text{Lg})$  3 and 4. The sample uncertainty is about  $\pm 1\%$ .

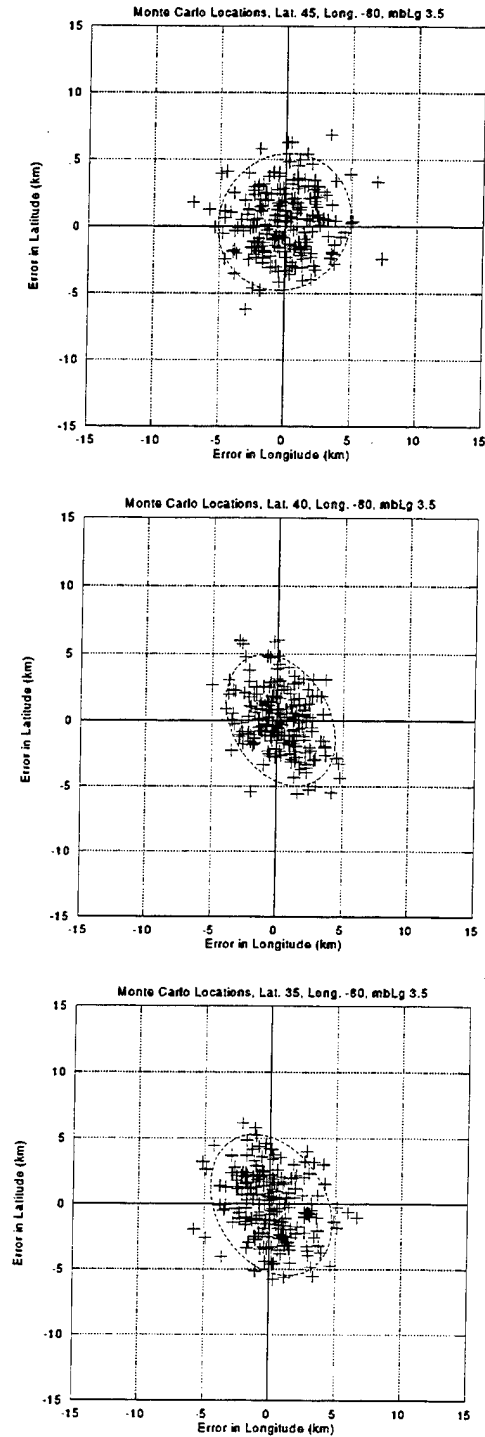


Figure 23 a,b,c. Monte Carlo locations for 35N (bottom), 40N (middle), and 45N (top) at 85W for  $m_b(Lg) = 3.5 \pm 0.1$ . The 90% confidence ellipse is drawn for each ensemble of realizations. There are approximately 200 to 300 events on each plot. Comparing these locations to 90% confidence error ellipses derived from the Monte Carlo procedure, we find that about 10% of the events lie outside the error ellipses.

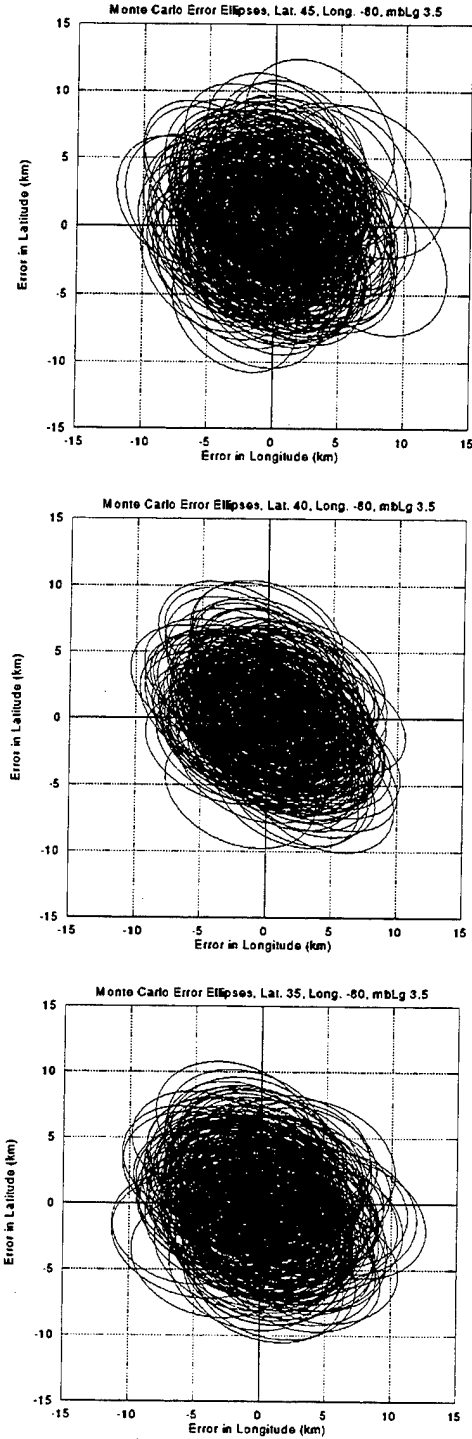


Figure 24 a,b,c. Monte Carlo locations for 35N (bottom), 40N (middle), and 45N (top) at 85W for  $m_b(Lg) = 3.5 \pm 0.1$ . The formal 90% confidence ellipse is drawn for each realization. There are approximately 200 to 300 events on each plot. Between 75% and 85% of the error ellipses contain the true location. The error ellipses are generally smaller than those shown in Figure 23.



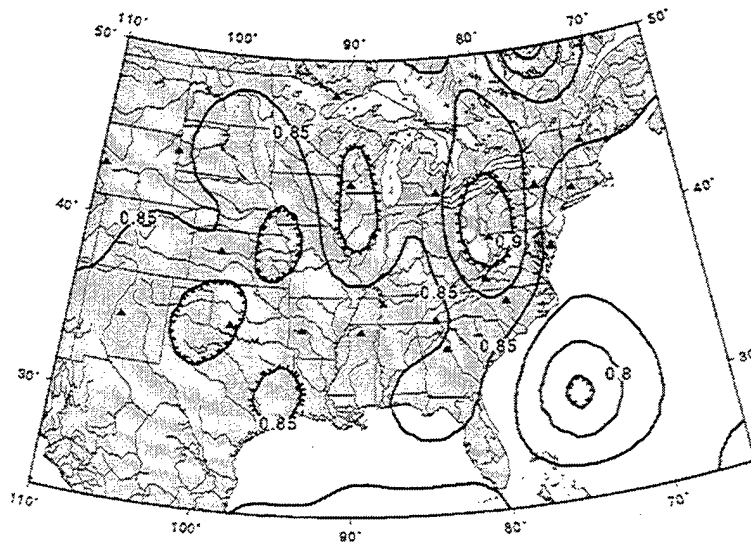


Figure 25. Map showing contours of the percentage of true locations contained within the formal errors of a Monte Carlo simulation of synthetic events with  $3.0 < m_b(Lg) < 4.2$ . Sampling uncertainty is better than  $\pm 1\%$  across most of the map.

If the distribution of errors was different from the assumed Chi-Squared distribution, then we might have tails of the distribution contaminated by a few “bad” locations and hence underestimates of the 90% confidence bounds. However, when we examine the Monte Carlo produced errors and compare them to the best fitting Chi-squared distribution in Figure 26, we find that the cumulative distribution of errors produced by the fully non-linear network simulation are indistinguishable from Chi-squared. Therefore, while the formal procedure assumes the right shape of the error distribution, it underestimates the scaling represented by the “curvature matrix.”

This simple result has interesting consequences. Nearly all location programs cite formal confidence ellipses derived from linearization of the non-linear estimation problem. It appears the curvature of the objective function is sometimes overestimated. The objective function is often flatter than estimated near the minimum, and therefore formal confidence bounds are often too small.

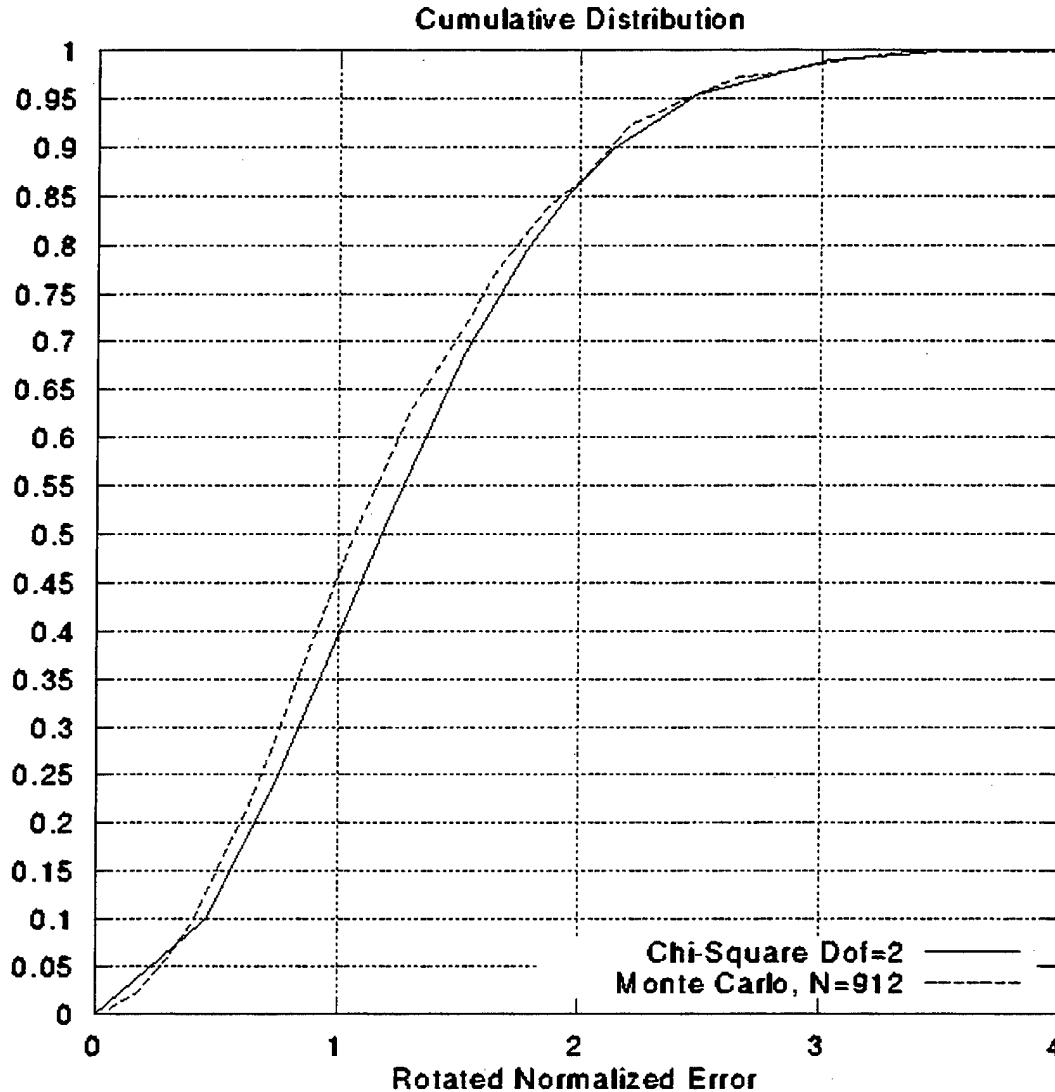


Figure 26. Comparison of the normalized cumulative errors to those predicted by a best fitting Chi-squared distribution. The non-linear Monte Carlo distribution did not generate excessive errors in the tails or a skewed distribution of error. While the formal methods underestimate the bounds, they appear to assume the correct shape of the error distribution.

## Conclusions

We have used an extensive compilation and analysis of source and propagation parameters for the Middle East/North Africa to simulate network detection and identification performance of the proposed IMS. Conclusions from this study include the following:

1. Performance is strongly influenced by source and propagation properties and by station coverage. Regions of very low  $Q$  are the most important features controlling detection and therefore location. Variations in  $Q$  and its frequency dependence are additionally important to the identification performance of the spectral slope discriminant. Because there are large variations in apparent

relative excitation of Lg and P, the identification performance of the Lg/P discriminant varies significantly throughout the region.

2. Expected identification levels at  $m_b=4$  or log-moment=14 Nt-m range from 0 to 100% in the region.
3. It is important to realize that in a heterogeneous region, the interpretation of network simulation results in terms of magnitude may be the quite inaccurate, to the extent that larger magnitude thresholds may indicate smaller source sizes. It is preferable to present the results in terms of source size (e.g. moment or yield).
4. It is possible to collect for this region an adequate data set which predicts the most important features of wave propagation there. Such a data set could be used to calibrate and adjust the analysis procedures of the IMS. Without adequate calibrations, the network performance will be spotty. **Xnice** can be used to evaluate calibration procedures or results and to evaluate changes in station coverage.
5. Formal error ellipses tend to underestimate location uncertainty, apparently because the linearization approximation to the iterative least-squares procedure overestimated the curvature of the  $L_2$  norm at the least-squares solution position. This systematic bias in so-called "90% error ellipses" actually may be providing "95%" to "85%" error ellipses in practice. A more detailed study of IDC procedures with proposed IMS stations is required to assess this important bias.

## References

- Abercrombie, Rachel E. (1995), "Earthquake Source Scaling Relationships from -1 to 5  $M_L$  Using Seismograms Recorded at 2.5-km Depth," *J. Geophys. Res.*, **100**, pp. 24,015-24,036.
- Baker, G.E. and T.G. Barker (1997), "Source and Propagation Characteristics for Network Performance Simulations in the Middle East," presented to DSWA Symposium on Monitoring a Comprehensive Test Ban Treaty, Orlando, FL.
- Barker, T.G. (1996), "**Xnice**: A System for Assessing Network Identification Performance," S-CUBED Scientific Report No.2 to Phillips Laboratory, PL-TR-96-2087, ADA321938.
- Barker, T.G. (1996), "Advanced Systems for Assessing the Performance of Regional Networks," *Proceedings of the 18<sup>th</sup> Annual Seismic Research Symposium on Monitoring a Comprehensive Test Ban Treaty*, edited by J.F. Lewkowicz, J.M. McPhetres and D.T. Reiter, Annapolis MD.
- Baumgardt, D. (1996), "Investigation of Lg Blockage and the Transportability of Regional Discriminants in the Middle East," Phillips Laboratory Scientific Report PL-TR-96-2294, ADA323818.

- Brune, James N. (1970), "Tectonic Stress and the Spectra of Seismic Shear Waves from Earthquakes," *J. Geophys. Res.*, **75**, pp. 4997-5009.
- El-Isa, Z.H. and A. Al Shanti (1989), "Seismicity and Tectonics of the Red Sea and Western Arabia," *Geophys. J. Intl.*, **97**, pp. 449-457.
- Gettings, M.E., H.R. Blank Jr., W. Mooney, and J. Healy (1986), "Crustal Structure of Southwestern Saudi Arabia," *J. Geophys. Res.*, **86**, pp. 6491-6512.
- Grant, L., F. Ryall, and W. Rivers (1996), "Ground Truth Database: ILPA/MAIO Handbook," Phillips Laboratory Scientific Report PL-TR-96-2236, ADA31955.
- Hanks, T. C. and H. Kanamori (1979), "A Moment Magnitude Scale," *J. Geophys. Res.*, **84**, pp. 2348-2350.
- Madariaga, R. (1976), "Dynamics of an Expanding Circular Fault," *Bull. Seism. Soc. Am.*, **66**, pp. 639-666.
- McLaughlin, K.L., T.G. Barker, and T.J. Bennett (1997), "Simulation of United States National Seismic Network Capabilities," Maxwell Technologies Final Report MFD-TR-97-15804 submitted to the Nuclear Regulatory Commission, NUREG/CR-6448, 2, May.
- Mitchell, Brian, Y. Pan, and J. Xie (1997), "Lg Coda Q Variation Across Eurasia and Its Relation to Continental Evolution," *manuscript submitted for publication*.
- Nuttli, O. (1973), "Seismic Wave Attenuation and Magnitude Relations for Eastern North America," *J. Geophys. Res.*, **78**, pp. 876-885.
- Rodgers, Arthur, J. Ni, and T. Hearn (1997), "Propagation Characteristics of Short-Period Sn and Lg in the Middle East," *Bull. Seism. Soc. Am.*, **87**, pp. 396-413.
- Shapira, A., and A. Hofstetter (1993), "Source Parameters and Scaling Relationships of Earthquakes in Israel," *Tectonophysics*, **217**, pp. 217-226.
- Su, F., K. Aki, T. Teng, Y. Zeng, S. Koyanagi, and K. Mayeda (1992), "The Relation Between Site Amplification Factor and Surficial Geology in Central California," *Bull. Seism. Soc. Am.*, **82**, pp. 580-602.
- Vernon, F., R. Mellors, J. Berger, A. M. Al-Amri, and J. Zollweg (1996), "Initial Results from the Deployment of Broadband Seismometers in the Saudi Arabian Shield," *Proceedings of the 18<sup>th</sup> Annual Seismic Research Symposium on Monitoring a Comprehensive Test Ban Treaty*, PL-TR-96-2153, ADA313692, pp. 108-117.
- Xie, Jiakang, and B. Mitchell (1990), "A Back-Projection Method for Imaging Large-Scale Lateral Variations of Lg Coda Q with Application to Continental Africa," *Geophys. J. Intl.*, **100**, pp. 161-181.

THOMAS AHRENS  
SEISMOLOGICAL LABORATORY 252-21  
CALIFORNIA INST. OF TECHNOLOGY  
PASADENA, CA 91125

AIR FORCE RESEARCH LABORATORY  
ATTN: VSOE  
29 RANDOLPH ROAD  
HANSCOM AFB, MA 01731-3010 (2 COPIES)

AIR FORCE RESEARCH LABORATORY  
ATTN: RESEARCH LIBRARY/TL  
5 WRIGHT STREET  
HANSCOM AFB, MA 01731-3004

AIR FORCE RESEARCH LABORATORY  
ATTN: AFRL/SUL  
3550 ABERDEEN AVE SE  
KIRTLAND AFB, NM 87117-5776 (2 COPIES)

RALPH ALEWINE  
NTPO  
1901 N. MOORE STREET, SUITE 609  
ARLINGTON, VA 22209

MUAWIA BARAZANGI  
INSTOC  
3126 SNEE HALL  
CORNELL UNIVERSITY  
ITHACA, NY 14853

G. ELI BAKER  
MAXWELL TECHNOLOGIES  
8888 BALBOA AVE.  
SAN DIEGO, CA 92123-1506

DOUGLAS BAUMGARDT  
ENSCO INC.  
5400 PORT ROYAL ROAD  
SPRINGFIELD, VA 22151

THERON J. BENNETT  
MAXWELL TECHNOLOGIES  
11800 SUNRISE VALLEY  
SUITE 1212  
RESTON, VA 22091

WILLIAM BENSON  
NAS/COS  
ROOM HA372  
2001 WISCONSIN AVE. NW  
WASHINGTON DC 20007

JONATHAN BERGER  
UNIV. OF CALIFORNIA, SAN DIEGO  
SCRIPPS INST. OF OCEANOGRAPHY IGPP, 0225  
9500 GILMAN DRIVE  
LA JOLLA, CA 92093-0225

ROBERT BLANDFORD  
AFTAC  
1300 N. 17TH STREET  
SUITE 1450  
ARLINGTON, VA 22209-2308

LESLIE A. CASEY  
DEPT. OF ENERGY/NN-20  
1000 INDEPENDENCE AVE. SW  
WASHINGTON DC 20585-0420

CENTER FOR MONITORING RESEARCH  
ATTN: LIBRARIAN  
1300 N. 17th STREET, SUITE 1450  
ARLINGTON, VA 22209

ANTON DAINTY  
HQ DSWA/PMA  
6801 TELEGRAPH ROAD  
ALEXANDRIA, VA 22310-3398

CATHERINE DE GROOT-HEDLIN  
UNIV. OF CALIFORNIA, SAN DIEGO  
IGPP  
8604 LA JOLLA SHORES DRIVE  
SAN DIEGO, CA 92093

DIANE DOSER  
DEPT. OF GEOLOGICAL SCIENCES  
THE UNIVERSITY OF TEXAS AT EL PASO  
EL PASO, TX 79968

DTIC  
8725 JOHN J. KINGMAN ROAD  
FT BELVOIR, VA 22060-6218 (2 COPIES)

MARK D. FISK  
MISSION RESEARCH CORPORATION  
735 STATE STREET  
P.O. DRAWER 719  
SANTA BARBARA, CA 93102-0719

LORI GRANT  
MULTIMAX, INC.  
311C FOREST AVE. SUITE 3  
PACIFIC GROVE, CA 93950

HENRY GRAY  
SMU STATISTICS DEPARTMENT  
P.O. BOX 750302  
DALLAS, TX 75275-0302

I. N. GUPTA  
MULTIMAX, INC.  
1441 MCCORMICK DRIVE  
LARGO, MD 20774

DAVID HARKRIDER  
BOSTON COLLEGE  
INSTITUTE FOR SPACE RESEARCH  
140 COMMONWEALTH AVENUE  
CHESTNUT HILL, MA 02167

THOMAS HEARN  
NEW MEXICO STATE UNIVERSITY  
DEPARTMENT OF PHYSICS  
LAS CRUCES, NM 88003

MICHAEL HEDLIN  
UNIVERSITY OF CALIFORNIA, SAN DIEGO  
SCRIPPS INST. OF OCEANOGRAPHY  
9500 GILMAN DRIVE  
LA JOLLA, CA 92093-0225

DONALD HELMBERGER  
CALIFORNIA INST. OF TECHNOLOGY  
DIV. OF GEOL. & PLANETARY SCIENCES  
SEISMOLOGICAL LABORATORY  
PASADENA, CA 91125

EUGENE HERRIN  
SOUTHERN METHODIST UNIVERSITY  
DEPT. OF GEOLOGICAL SCIENCES  
DALLAS, TX 75275-0395

ROBERT HERRMANN  
ST. LOUIS UNIVERSITY  
DEPT. OF EARTH & ATMOS. SCIENCES  
3507 LACLEDE AVENUE  
ST. LOUIS, MO 63103

VINDELL HSU  
HQ/AFTAC/TTR  
1030 S. HIGHWAY A1A  
PATRICK AFB, FL 32925-3002

RONG-SONG JIH  
HQ DSWA/PMA  
6801 TELEGRAPH ROAD  
ALEXANDRIA, VA 22310-3398

THOMAS JORDAN  
MASS. INST. OF TECHNOLOGY  
BLDG 54-918  
CAMBRIDGE, MA 02139

LAWRENCE LIVERMORE NAT'L LAB  
ATTN: TECHNICAL STAFF (PLS ROUTE)  
PO BOX 808, MS L-175  
LIVERMORE, CA 94551

LAWRENCE LIVERMORE NAT'L LAB  
ATTN: TECHNICAL STAFF (PLS ROUTE)  
PO BOX 808, MS L-208  
LIVERMORE, CA 94551

LAWRENCE LIVERMORE NAT'L LAB  
ATTN: TECHNICAL STAFF (PLS ROUTE)  
PO BOX 808, MS L-202  
LIVERMORE, CA 94551

LAWRENCE LIVERMORE NAT'L LAB  
ATTN: TECHNICAL STAFF (PLS ROUTE)  
PO BOX 808, MS L-205  
LIVERMORE, CA 94551

LAWRENCE LIVERMORE NAT'L LAB  
ATTN: TECHNICAL STAFF (PLS ROUTE)  
PO BOX 808, MS L-200  
LIVERMORE, CA 94551

LAWRENCE LIVERMORE NAT'L LAB  
ATTN: TECHNICAL STAFF (PLS ROUTE)  
PO BOX 808, MS L-221  
LIVERMORE, CA 94551

THORNE LAY  
UNIV. OF CALIFORNIA, SANTA CRUZ  
EARTH SCIENCES DEPARTMENT  
EARTH & MARINE SCIENCE BUILDING  
SANTA CRUZ, CA 95064

ANATOLI L. LEVSHIN  
DEPARTMENT OF PHYSICS  
UNIVERSITY OF COLORADO  
CAMPUS BOX 390  
BOULDER, CO 80309-0309

JAMES LEWKOWICZ  
WESTON GEOPHYSICAL CORP.  
325 WEST MAIN STREET  
NORTHBORO, MA 01532

LOS ALAMOS NATIONAL LABORATORY  
ATTN: TECHNICAL STAFF (PLS ROUTE)  
PO BOX 1663, MS F659  
LOS ALAMOS, NM 87545

LOS ALAMOS NATIONAL LABORATORY  
ATTN: TECHNICAL STAFF (PLS ROUTE)  
PO BOX 1663, MS F665  
LOS ALAMOS, NM 87545

LOS ALAMOS NATIONAL LABORATORY  
ATTN: TECHNICAL STAFF (PLS ROUTE)  
PO BOX 1663, MS C335  
LOS ALAMOS, NM 87545

GARY MCCARTOR  
SOUTHERN METHODIST UNIVERSITY  
DEPARTMENT OF PHYSICS  
DALLAS, TX 75275-0395

KEITH MCLAUGHLIN  
CENTER FOR MONITORING RESEARCH  
SAIC  
1300 N. 17TH STREET, SUITE 1450  
ARLINGTON, VA 22209

BRIAN MITCHELL  
DEPARTMENT OF EARTH & ATMOSPHERIC SCIENCES  
ST. LOUIS UNIVERSITY  
3507 LACLEDE AVENUE  
ST. LOUIS, MO 63103

RICHARD MORROW  
USACDA/IVI  
320 21ST STREET, N.W.  
WASHINGTON DC 20451

JOHN MURPHY  
MAXWELL TECHNOLOGIES  
11800 SUNRISE VALLEY DRIVE  
SUITE 1212  
RESTON, VA 22091

JAMES NI  
NEW MEXICO STATE UNIVERSITY  
DEPARTMENT OF PHYSICS  
LAS CRUCES, NM 88003

ROBERT NORTH  
CENTER FOR MONITORING RESEARCH  
1300 N. 17th STREET, SUITE 1450  
ARLINGTON, VA 22209

OFFICE OF THE SECRETARY OF DEFENSE  
DDR&E  
WASHINGTON DC 20330

JOHN ORCUTT  
INST. OF GEOPH. & PLANETARY PHYSICS  
UNIV. OF CALIFORNIA, SAN DIEGO  
LA JOLLA, CA 92093

PACIFIC NORTHWEST NAT'L LAB  
ATTN: TECHNICAL STAFF (PLS ROUTE)  
PO BOX 999, MS K6-48  
RICHLAND, WA 99352

PACIFIC NORTHWEST NAT'L LAB  
ATTN: TECHNICAL STAFF (PLS ROUTE)  
PO BOX 999, MS K6-40  
RICHLAND, WA 99352

PACIFIC NORTHWEST NAT'L LAB  
ATTN: TECHNICAL STAFF (PLS ROUTE)  
PO BOX 999, MS K6-84  
RICHLAND, WA 99352

PACIFIC NORTHWEST NAT'L LAB  
ATTN: TECHNICAL STAFF (PLS ROUTE)  
PO BOX 999, MS K5-12  
RICHLAND, WA 99352

FRANK PILOTTE  
HQ AFTAC/TT  
1030 S. HIGHWAY A1A  
PATRICK AFB, FL 32925-3002

KEITH PRIESTLEY  
DEPARTMENT OF EARTH SCIENCES  
UNIVERSITY OF CAMBRIDGE  
MADINGLEY RISE, MADINGLEY ROAD  
CAMBRIDGE, CB3 0EZ UK

JAY PULLI  
BBN SYSTEMS AND TECHNOLOGIES, INC.  
1300 NORTH 17TH STREET  
ROSSLYN, VA 22209

DELAINE REITER  
AFRL/VSOE (SENCOM)  
73 STANDISH ROAD  
WATERTOWN, MA 02172

PAUL RICHARDS  
COLUMBIA UNIVERSITY  
LAMONT-DOHERTY EARTH OBSERV.  
PALISADES, NY 10964

MICHAEL RITZWOLLER  
DEPARTMENT OF PHYSICS  
UNIVERSITY OF COLORADO  
CAMPUS BOX 390  
BOULDER, CO 80309-0309

DAVID RUSSELL  
HQ AFTAC/TTR  
1030 SOUTH HIGHWAY A1A  
PATRICK AFB, FL 32925-3002

CHANDAN SAIKIA  
WOODWARD-CLYDE FED. SERVICES  
566 EL DORADO ST., SUITE 100  
PASADENA, CA 91101-2560

SANDIA NATIONAL LABORATORY  
ATTN: TECHNICAL STAFF (PLS ROUTE)  
DEPT. 5704  
MS 0979, PO BOX 5800  
ALBUQUERQUE, NM 87185-0979

SANDIA NATIONAL LABORATORY  
ATTN: TECHNICAL STAFF (PLS ROUTE)  
DEPT. 9311  
MS 1159, PO BOX 5800  
ALBUQUERQUE, NM 87185-1159

SANDIA NATIONAL LABORATORY  
ATTN: TECHNICAL STAFF (PLS ROUTE)  
DEPT. 5704  
MS 0655, PO BOX 5800  
ALBUQUERQUE, NM 87185-0655

SANDIA NATIONAL LABORATORY  
ATTN: TECHNICAL STAFF (PLS ROUTE)  
DEPT. 5736  
MS 0655, PO BOX 5800  
ALBUQUERQUE, NM 87185-0655

THOMAS SERENO JR.  
SAIC  
10260 CAMPUS POINT DRIVE  
SAN DIEGO, CA 92121

AVI SHAPIRA  
SEISMOLOGY DIVISION  
IPRG  
P.O.B. 2286 NOLON 58122 ISRAEL

ROBERT SHUMWAY  
410 MRAK HALL  
DIVISION OF STATISTICS  
UNIVERSITY OF CALIFORNIA  
DAVIS, CA 95616-8671

MATTHEW SIBOL  
ENSCO, INC.  
445 PINEDA CT.  
MELBOURNE, FL 32940

DAVID SIMPSON  
IRIS  
1200 NEW YORK AVE., NW  
SUITE 800  
WASHINGTON DC 20005

JEFFRY STEVENS  
MAXWELL TECHNOLOGIES  
8888 BALBOA AVE.  
SAN DIEGO, CA 92123-1506

BRIAN SULLIVAN  
BOSTON COLLEGE  
INSITUTE FOR SPACE RESEARCH  
140 COMMONWEALTH AVENUE  
CHESTNUT HILL, MA 02167

TACTEC  
BATTELLE MEMORIAL INSTITUTE  
505 KING AVENUE  
COLUMBUS, OH 43201 (FINAL REPORT)

NAFI TOKSOZ  
EARTH RESOURCES LABORATORY  
M.I.T.  
42 CARLTON STREET, E34-440  
CAMBRIDGE, MA 02142

LAWRENCE TURNBULL  
ACIS  
DCI/ACIS  
WASHINGTON DC 20505

GREG VAN DER VINK  
IRIS  
1200 NEW YORK AVE., NW  
SUITE 800  
WASHINGTON DC 20005



FRANK VERNON  
UNIV. OF CALIFORNIA, SAN DIEGO  
SCRIPPS INST. OF OCEANOGRAPHY  
9500 GILMAN DRIVE  
LA JOLLA, CA 92093-0225

JILL WARREN  
LOS ALAMOS NATIONAL LABORATORY  
GROUP NIS-8  
P.O. BOX 1663  
LOS ALAMOS, NM 87545      (5 COPIES)

RU SHAN WU  
UNIV. OF CALIFORNIA, SANTA CRUZ  
EARTH SCIENCES DEPT.  
1156 HIGH STREET  
SANTA CRUZ, CA 95064

JAMES E. ZOLLWEG  
BOISE STATE UNIVERSITY  
GEOSCIENCES DEPT.  
1910 UNIVERSITY DRIVE  
BOISE, ID 83725

TERRY WALLACE  
UNIVERSITY OF ARIZONA  
DEPARTMENT OF GEOSCIENCES  
BUILDING #77  
TUCSON, AZ 85721

DANIEL WEILL  
NSF  
EAR-785  
4201 WILSON BLVD., ROOM 785  
ARLINGTON, VA 22230

JIANG XIE  
COLUMBIA UNIVERSITY  
LAMONT DOHERTY EARTH OBSERV.  
ROUTE 9W  
PALISADES, NY 10964